Pure Appl. Chem., Vol. 76, No. 6, pp. 1161–1213, 2004.
© 2004 IUPAC

INTERNATIONAL UNION OF PURE AND APPLIED CHEMISTRY

ANALYTICAL CHEMISTRY DIVISION*

CRITICAL EVALUATION OF THE STATE OF THE ART OF THE ANALYSIS OF LIGHT ELEMENTS IN THIN FILMS DEMONSTRATED USING THE EXAMPLES OF SiO_XN_Y AND AlO_XN_Y FILMS

(IUPAC Technical Report)

Prepared for publication by
SABINE DREER[1,‡] AND PETER WILHARTITZ[2]

[1]*Institute of Chemical Technologies and Analytics, Vienna University of Technology, Getreidemarkt 9/164-AC, A-1060 Wien, Austria;* [2]*Plansee AG, Thin Film Technology, A-6600 Reutte, Austria*

*Membership of the Analytical Chemistry Division during the final preparation of this report (2002–2003) was as follows:

***President*:** D. Moore (USA); ***Titular Members*:** F. Ingman (Sweden); K. J. Powell (New Zealand); R. Lobinski (France); G. G. Gauglitz (Germany); V. P. Kolotov (Russia); K. Matsumoto (Japan); R. M. Smith (UK); Y. Umezawa (Japan); Y. Vlasov (Russia); ***Associate Members*:** A. Fajgelj (Slovenia); H. Gamsjäger (Austria); D. B. Hibbert (Australia); W. Kutner (Poland); K. Wang (China); ***National Representatives*:** E. A. G. Zagatto (Brazil); M.-L. Riekkola (Finland); H. Kim (Korea); A. Sanz-Medel (Spain); T. Ast (Yugoslavia).

‡Corresponding author

Republication or reproduction of this report or its storage and/or dissemination by electronic means is permitted without the need for formal IUPAC permission on condition that an acknowledgment, with full reference to the source, along with use of the copyright symbol ©, the name IUPAC, and the year of publication, are prominently visible. Publication of a translation into another language is subject to the additional condition of prior approval from the relevant IUPAC National Adhering Organization.

Critical evaluation of the state of the art of the analysis of light elements in thin films demonstrated using the examples of SiO_XN_Y and AlO_XN_Y films

(IUPAC Technical Report)

Abstract: The quantitative analysis of thin films containing light elements is very important in improving the coating processes and technological properties of the products. In order to review the state of the art of modern analytical techniques for such applications, the model systems SiO_XN_Y and AlO_XN_Y were selected. Over 1000 abstracts were screened, and the relevant literature was evaluated to give a comprehensive overview of instruments, analytical procedures and results, film types, deposition methods, and investigation goals. From more than 150 citations, the limitations, drawbacks, and pitfalls of the different methods were extracted and reviewed critically, while in addition, improvements were proposed where possible. These suggestions are combined with the newest results of investigation by the authors of this paper. Recommendations concerning the optimized combination of analytical methods for different analytical problems have been worked out on the basis of all results. Analysis of various multicomponent systems containing light elements demonstrated the applicability of the different methods of analysis in combination to all film systems with related compositions.

CONTENTS

LIST OF ABBREVIATIONS
1. INTRODUCTION
2. OPTICAL TECHNIQUES
   2.1 Ellipsometry
   2.2 Spectrophotometry
3. RESONANCE METHODS
   3.1 Infrared spectrometry
   3.2 Raman scattering
   3.3 Electron spin resonance
   3.4 Photoluminescence
4. X-RAY ANALYTICAL TECHNIQUES
   4.1 X-ray photoelectron spectrometry
   4.2 X-ray excited Auger electron spectrometry
   4.3 X-ray diffraction
   4.4 X-ray reflectometry
   4.5 Grazing incidence X-ray scattering
   4.6 Grazing emission X-ray fluorescence spectrometry
   4.7 Extended X-ray absorption fine structure
   4.8 X-ray absorption near-edge structure
5. ELECTRON BEAM ANALYTICAL TECHNIQUES
   5.1 Electron probe microanalysis
   5.2 Auger electron spectrometry
   5.3 Electron microscopy
   5.4 Electron energy loss spectrometry
6. ION BEAM ANALYTICAL TECHNIQUES
   6.1 Rutherford backscattering spectrometry
   6.2 Elastic recoil detection analysis
   6.3 Nuclear reaction analysis
7. PHOTON ACTIVATION ANALYSIS
8. SPUTTERING TECHNIQUES
   8.1 Secondary ion mass spectrometry
   8.2 High-frequency, secondary neutral mass spectrometry
   8.3 High-frequency, glow discharge optical emission spectrometry
9. MECHANICAL TECHNIQUES
   9.1 Stylus measurement
   9.2 Atomic force microscopy
   9.3 Hardness and elastic constants determination
   9.4 Nano-indentation
   9.5 Tribological testing
   9.6 Adhesion testing
10. SPECIAL METHODS
   10.1 Hot gas extraction
   10.2 Weighing
   10.3 Sink-float method
11. CONCLUSIONS
12. REFERENCES

LIST OF ABBREVIATIONS

AES	Auger electron spectrometry
AFM	atomic force microscopy
AR-XPS	angle-resolved XPS
ATR	attenuated total reflection
CMA	cylindrical mirror analyzer
CVD	chemical vapor deposition
EDS/EDX	energy-dispersive X-ray spectrometry
EELS	electron energy loss spectrometry
EMA	effective media approximation
EPMA	electron probe microanalysis
ERDA	elastic recoil detection analysis
ESCA	electron spectroscopy for chemical analysis (= XPS)
ESR	electron spin resonance
EXAFS	extended X-ray absorption fine structure
FTIR	Fourier transform infrared
GDOES	glow discharge optical emission spectrometry
hf-GDOES	high-frequency GDOES
HFS	hydrogen forward scattering spectrometry
HREELS	high-resolution electron energy loss spectrometry
HR-TEM	high-resolution TEM
IBAD	ion beam-assisted deposition
IR	infrared
IRRAS	infrared reflection absorption spectrometry
LEED	low-energy electron diffraction
LEEIXS	low-electron energy-induced X-ray spectrometry
LPCVD	low-pressure CVD
NIR	near infrared
NRA	nuclear reaction analysis
NRRA	nuclear resonance reaction analysis
PAA	photon activation analysis
PECVD	plasma-enhanced CVD
PL	photoluminescence
RBM	random bonding model
RBS	Rutherford backscattering spectrometry
REELS	reflection electron energy loss spectrometry
RHEED	reflection high-energy electron diffraction
RMM	random mixture model
SE	spectroscopic ellipsometry
SEM	scanning electron microscopy
SIMS	secondary ion mass spectrometry
SNMS	secondary neutral mass spectrometry or sputtered neutral mass spectrometry
STM	scanning tunneling microscopy
TEM	transmission electron microscopy
TGA	thermogravimetric analysis
TOF-SIMS	time-of-flight SIMS
UHV	ultrahigh vacuum
UPS	ultraviolet photoelectron spectrometry
UV	ultraviolet

VASE	variable-angle spectroscopic ellipsometry
VIS	visible absorption spectrometry
WDS/WDX	wavelength-dispersive X-ray spectrometry
XAES	X-ray excited AES
XANES	X-ray absorption near-edge structure
XPS	X-ray photoelectron spectrometry (= ESCA)
XRD	X-ray diffraction
XRF	X-ray fluorescence

1. INTRODUCTION

Coatings consisting of a metal compound with one or more light elements like B, C, N, and O have been used for several decades because of their outstanding performance in areas such as hardness, corrosion behavior, wear resistance, and optical as well as electrical properties. However, owing to pronounced environmental concerns and increasing demand for high-performance parts in many technological applications like electronics, data storage, optics, tools, automotive, aerospace, etc., but also in consumer products like pens, fittings, handles, fashion accessories, etc., the market for such coatings currently exhibits a twofold or higher growth rate per year. Despite the enormously growing importance of such coatings, specific development and correlation of the properties vs. chemical composition is very difficult because of the lack of appropriate reference materials.

For this reason, this review tries to give a comprehensive overview of the analytical techniques used so far. The authors, on the basis of their own work and experience, will try to assess the literature and give suggestions for the selection of a proper analytical approach.

Aluminum and silicon oxynitride films were chosen for this publication in place of other films containing light elements since all relevant problems occurring during analysis can be demonstrated with these three-component films. The insulating properties of the films result in charging, and oxidation of the surface also has to be considered. The transparency of stoichiometric films makes it necessary to include optical properties in the investigation. Furthermore, these film materials can be used as protective layers against scratching and as diffusion barriers, thus requiring evaluation of mechanical properties such as hardness.

Since the number of thin film analytical methods applied on silicon and aluminum oxynitride films is immense, the methods are classified in the following by the way the signal is generated.

SiO_XN_Y and AlO_XN_Y films with homogeneous composition over the whole film thickness can be analyzed by bulk analytical methods, which do not give information on the depth distribution. However, many deposition methods do not produce homogeneous films, and sometimes films are deposited deliberately with varying composition, for example, Rugate filters. Also, the deposited films can be altered at the surface by oxidation. In [1], a change of the refractive index was observed after exposure of the films to air. This effect was attributed to the diffusion of oxygen through the low-density films, followed by the formation of Si–O bonds, which have a higher bonding probability than Si–N bonds. In order to fully prove such conclusions and to check the successful deposition of graded films, such films need to be analyzed by methods capable of resolving the depth distribution of silicon or aluminum, oxygen, and nitrogen in the films. Most of these techniques are based on the removal of the sample surface by sputtering.

Structural information is another goal in analytical thin film characterization. The structure of SiO_XN_Y and AlO_XN_Y films can be crystalline or amorphous and three different atomic bonding structures are theoretically possible. One possibility is the absolutely unordered bonding of Si or Al, O, and N in the films, including N–N bonds and other mostly unwanted bonds. The other two possibilities are cited frequently as the RBM (random bonding model) and RMM (random mixture model). The RBM describes the SiO_XN_Y films as tetrahedrally bonded Si atoms surrounded by oxygen and nitrogen in form of twofold-coordinated oxygen Si–O–Si and threefold-coordinated nitrogen Si–N–Si bonds, the

mean number of oxygen and nitrogen atoms surrounding one Si atom determining the composition of the film. N and O displace one another in a random manner in a disordered network of such SiN_ZO_{4-Z} tetrahedra. In the RMM, a mixture of two phases is suggested, in which silicon atoms are either bonded to four nitrogen or oxygen atoms, but nitrogen and oxygen cannot be bonded to the same silicon atom. The same considerations are valid for the threefold-coordinated aluminum atoms.

Publications dealing with different aspects of oxynitride film characterization obviously have to be laid out rather comprehensively and thus mostly have review character. One such paper on the characterization of LPCVD SiO_XN_Y films is [2]. NRA was applied for the determination of hydrogen utilizing the reaction $^{1}H(^{15}N, \alpha\gamma)^{12}C$, additionally, ERDA was used for hydrogen profiling, RBS was used for the quantification of oxygen and nitrogen, and IR spectra were evaluated. Another review by this author dealing with films produced by various deposition methods can be found in [3]. A review on oxynitride films without any detailed information concerning the analytical parameters is [4], where films produced by various deposition methods are investigated.

Because of the wide field of applications of oxynitride films, physical properties of the films are frequently investigated. Hardness and Young's modulus are the two mechanical properties that are examined frequently in addition to the two optical properties refractive index and absorption. Those properties are representative for other characteristics not taken into consideration in this publication.

Note: In the following descriptions, the term *absorption coefficient* always means the *linear napierian absorption coefficient,* α, with dimension of inverse length. In ellipsometry, it is customary to also define an *extinction coefficient, k*, defined as the dimensionless quantity $k = \alpha\lambda/4\pi$, where λ is the wavelength. See IUPAC's Physical Chemistry Division, *Quantities, Units and Symbols in Physical Chemistry*, prepared for publication by I. Mills, T. Cvitaš, K. Homann, N. Kallay, K. Kuchitsu, 2nd ed. Blackwell Science, Oxford (1988), Sect. 2.7, and A. Röseler, *Infrared Spectroscopic Ellipsometry*, Akademie-Verlag, Berlin (1990).

2. OPTICAL TECHNIQUES

The optical properties of oxynitride films can be exploited for the production of protective coatings for optical components, the fabrication of waveguides [5,6], antireflective layers [7,8] or barrier layers [9] in laser lithography, integrated optics for sensors [10], and so on. The most important reason for the interest in these materials is the possibility to vary the refractive index with the composition of the films and accomplish values between those of the oxide and the nitride. Therefore, very often the optical properties of oxynitride films are analyzed. Usually the correlation between one deposition parameter and the resulting optical properties is investigated. Some authors also state a linear correlation between the refractive index and the oxygen content in the films or ratios like O/(O+N), such as in [11–13], or find a slightly curved correlation [14], but no conclusive proof with sufficient data has been given for these assumptions. In [11], the rectilinear correlation between the refractive index and the oxygen content ends below oxygen contents <10 at% (atomic fraction), where the slope increases. In [7,8], diagrams of the real part and the imaginary part of the refractive index are given.

Some of the optical techniques can also be utilized for the determination of the film thickness. This can be especially advantageous for oxynitride films, since the quartz oscillator usually used is unreliable if the exact density and mechanical properties are not known, as is the case for the rather complicated SiO_XN_Y and AlO_XN_Y films [15].

2.1 Ellipsometry

Spectroscopic ellipsometry (SE) is often used to characterize the optical properties of films and the film thickness. A linearly polarized light incident at an oblique angle to the surface is reflected elliptically polarized. This new polarization state of the reflected light contains information about the sample prop-

erties and is determined by a polarizer. Two parameters, which are called Psi and Delta, characterize the polarization ellipse. Ψ expresses the amplitude ratio of the *p*- and *s*-polarized part of the radiation at the applied wavelength; Δ gives the phase difference. The measured data are numerically fitted.

In [16], the measurements were performed at room temperature with an automatic rotating analyzer ellipsometer at an incidence angle of 75° in the spectral range of 250–820 nm at 5 nm intervals. The beam diameter was approximately 1 mm. For the fitting of the experimental data, the optical behavior of the SiO_XN_Y films was described by the Bruggeman EMA as a dielectric physical mixture of two phases, SiO_2 and Si_3N_4, by utilizing their relative volume fractions. Since the films were inhomogeneous in depth according to AES results, several models for the profiles of the refractive index and the volume fractions were tested by fitting the experimental data. Finally, a depth profile of the optical constants with best fit was found, which was consistent with the AES depth profile but with an additional 3-nm-thick interfacial layer consisting of Si_3N_4 and Si. Since the SE data are sensitive to the refractive index depth profile and the film thickness, the authors describe it as a future tool for fast, quantitative, nondestructive, and if necessary in situ analytical tool for the analysis of Rugate filters and other optical systems. VASE measurements in air were performed by the same group of authors in [17] at incident angles of 70° and 72° over a wavelength range of 320–820 nm with a step-width of 10 nm. Here, the authors stress that the effective media approximation (EMA) is only a crude approximation while the films actually are most probably atomic mixtures of Si, O, and N. Since the results of this model were good, this discrepancy was not further checked. In an earlier publication [18], the optical properties of SiO_XN_Y and AlO_XN_Y films were investigated by spectral transmittance measured by a spectrophotometer. In this publication, a SiO_X sample was investigated ellipsometrically and the refractive index and the extinction coefficient of bulk SiO_2 and SiO are given in a diagram.

Ellipsometry measurements at 633 nm and spectrophotometric measurements over the range of 360–700 nm were combined in [19] for the characterization of SiO_2, Si_3N_4, and SiO_XN_Y films deposited by dc magnetron sputtering. Refractive index and thickness of the films were determined by ellipsometry, while absorption, transmittance, and reflectance were determined by spectrophotometry. The refractive index results were correlated with the deposition gas flows. The lowest achieved refractive index for SiO_2 films was 1.45 with no measurable absorption. The silicon nitride film with the highest refractive index of 2.27 and at the same time lowest absorption of still 19 % at 500 nm was defined as stoichiometric Si_3N_4. Substoichiometric silicon rich films did show a higher refractive index and higher absorbance, as was to be expected, and overstoichiometric Si_3N_4 films were produced with refractive indices down to 2.09. SiO_XN_Y produced by mixtures of oxygen and nitrogen gas showed refractive indices from 2.36 to 1.45. The transmission increased rapidly with decreasing refractive index. A transmission better than 70 % up to approximately 90 % was accomplished only for films with a refractive index lower than 1.66. The higher reactivity of oxygen was avoided by using nitrogen and air to deposit SiO_XN_Y films in a more controlled way with refractive indices of 2.33 to 1.60. The composition of the films was not determined by other methods of analysis.

Ellipsometry was also used in [20] to correlate the refractive index at 632.8 nm to the substrate temperature of a pulsed laser deposition process. An increase of the refractive index with increasing temperature and also increased film thickness was found. A correlation between the refractive index and either the oxygen gas flow or the composition was found. Likewise, in [21,22] an ellipsometer was used to measure the film thickness and the refractive index. The authors conclude that the O/N ratio of the films can be derived from the refractive index with a dependence according to the Bruggeman approximation (RMM). In a diagram, the refractive index ranging from 2.0 for the nitride to 1.46 for the oxide is given vs. the ratio of O/(O+N), and a slightly concave curve represents the theoretical Bruggeman approximation with assumed refractive indices and densities of SiO_2 and Si_3N_4. Rather doubtful is the conclusion that the thin native oxide layer on the silicon substrates no longer influences the refractive index if the films are thicker than 20 nm. In [23], a rectilinear correlation between the refractive index and the oxygen content in at% was observed, but only six samples were measured. The refractive index

at 634.8 nm determined by ellipsometry is given vs. x in the formula $(SiO_2)_X(Si_3N_4)_{1-X}$ and a straight-lined correlation was observed in [24]. A multi-wavelength (44 channels) spectroscopic ellipsometer was used. The refractive index varied between ~1.92 (x = 0) and ~1.45 (x = 1).

An in-depth profile of the refractive index was performed in [25] with an automatic Gaertner model L17 ellipsometer at an incidence angle of 70°. The refractive index was measured before and after etching of the films, which were deposited by PECVD and had a thickness of 100 nm. The refractive index ranging from ~1.93–1.58 vs. the oxygen content up to 35 at% exhibits a monotonous although not rectilinear dependence with a slightly concave curvature.

For ellipsometry measurements at one wavelength, the wavelength of 545.1 nm is sometimes used to determine the film thickness and the refractive index [26]. Of course, the growth rate can also be determined by ellipsometry, which was done in [27] with a Rudolf Research Auto-EL ellipsometer at 632.8 nm. In this publication, UV/VIS/NIR spectrophotometry was also utilized for the calculation of the optical band gap.

Optical characterization of silicon oxynitride films was performed in [28] in situ with a phase-modulated ellipsometer, while ex situ measurements were performed with a spectro-ellipsometer in the photon energy range of 1.5 to 5 eV. The films were deposited on (100) silicon wafers. The film composition was determined by AES and XPS without giving further information on the measurements. The refractive index varied between 1.47 and 2.05 (oxide to nitride) at 2.5 eV with negligible absorption. Time-dependent Ψ vs. Δ curves are shown and even void volume is calculated by EMA.

The refractive index, the thickness, and the surface homogeneity of AlO_XN_Y films deposited on GaAs were determined by ellipsometry with a Gaertner Model L117 instrument at 632.8 nm and the complex refractive index of the substrate was taken into account for the calculations [29]. From the observed refractive index, the atomic fraction of AlN in these films was calculated under the assumption that the refractive index varies linearly between 1.55 for Al_2O_3 and 2.18 for AlN. The film composition was also determined by AES and comparable results were obtained. The same instrument at the same wavelength was used in [30] together with a VASE instrument at 250 nm. The real refractive indices of SiO_XN_Y films and the extinction coefficient were determined. The refractive index was in the range of 1.71 for $SiO_{0,97}N_{0,79}$ to 2.396 for $SiO_{0,04}N_{0,90}$ at 250 nm, while the absorption coefficient varied from 0 to 0.812 for the nitrogen-rich film. The composition of the samples was determined by XPS.

The results published in [31] by our working group were obtained with a Sopra ES 4 G spectral ellipsometer, in the range of 300–850 nm. The same instrument was applied in [32], where the refractive index, absorption coefficient, and thickness of films deposited on silicon substrates were evaluated and the variation of tan Ψ, cos Δ, and the refractive index with wavelength was shown, as well as the polynomial fitting of the data. The Sellmeier model was used for the evaluations. The difficulties of these otherwise elegant techniques are rooted in the fitting procedures. Different models can and must be applied depending on the sample, and today this method is one of the most frequently applied optical techniques. With fitting equations for the obtained spectra, almost all film properties from composition to thickness and surface properties are determined by ellipsometry and described in the literature. Yet, for unknown samples only two to three properties can be evaluated reliably, otherwise the film properties have to be known in advance in order to obtain additional information.

Since the absorption of our films, which were produced by dc magnetron sputtering [33], was negligible, the fits were performed with zero absorption as a fitting parameter and the refractive index and the film thickness were obtained. The results obtained by this method were compared to other optical techniques in [34], and good correspondence was achieved. The refractive index data of [31] are based on these ellipsometry measurements. In this publication, refractive index vs. wavelength curves for different AlO_XN_Y film compositions are given, the dependence of the refractive index on the deposition parameters is evaluated statistically, including combined influences of parameters, and a rectilinear correlation between the refractive index and the oxygen concentration in the films is established.

Measurements with a single wavelength ellipsometer resulted in the insight that this instrument is only useful for in situ measurements during deposition, but otherwise does not deliver useful results

if great pains are not taken for special sample production with graded thickness and the mathematical evaluation.

2.2 Spectrophotometry

Spectrophotometry is a technique that allows calculation of properties like refractive index and absorption. Monochromatized light illuminates the sample, and usually the measurement is performed in transmittance. In the case of samples that are impermeable to radiation in the wavelength range used, the intensity of the reflected beam is recorded. This measurement is performed by an instrument scanning the wavelength range of interest. The part of the beam reflected at the sample surface and the part reflected at the interface between transparent film and opaque substrate interfere and these interference fringes are recorded vs. wavelength. The intensity vs. wavelength plots for the films can then be compared to the spectra of the clean substrates. If the films are only weakly absorbing, the difference in the position of the intensity maxima and minima or the envelope of the curves can be evaluated [35,36]. For absorbing samples, different approaches have to be used [37].

For transparent samples, optical transmission spectra are very commonly used to investigate the optical properties of films. In [38], a double beam spectrophotometer was used to investigate samples with a thickness of 350 nm at the neighborhood of the fundamental absorption edge in the 0.4–2.5 μm wavelength range. The observed spectra, which should deliver the absorption coefficient and the optical gap, were not fully analyzed, because interference fringes were introduced by the films. The authors of this article did not know how to evaluate such transmission curves.

Optical transmission spectra were recorded with a Varian 2300 spectrometer in order to gain information on the band edge in [39]. A strong shift in the band edge to shorter wavelengths was observed for increasing hydrogen contents. The spectra were recorded in the range of 180–400 nm. It was possible to vary the band gap continuously with the oxygen-to-nitrogen ratio between the values for pure Si_3N_4 and SiO_2. The curve shapes were influenced by interference effects and the different film thicknesses. The refractive index vs. wavelength in the range of 150–400 nm was calculated in [40] together with the optical absorption from reflectance and transmittance studies at normal incidence.

The refractive index and the film thickness of AlO_XN_Y and SiO_XN_Y deposited by reactive ion beam sputter deposition were determined in [41] by optical transmittance in the wavelength range of 200–800 nm by a dual beam spectrophotometer. The refractive index was also determined by spectroscopic ellipsometry in the range of 400–800 nm and the thickness monitored by a quartz crystal oscillator. The spectral variation of the refractive index of several AlO_XN_Y and SiO_XN_Y films is given in diagrams and the possibility to control the refractive index of the films by varying the mass flow of the oxygen gas was studied. Some multilayer optical coatings were produced in order to prove these results, such as high-reflectance films and antireflectance coatings.

Dual beam spectrophotometers were used for transmission measurements of SiO_XN_Y and AlO_XN_Y films deposited on fused silica (quartz) substrates and the refractive index was calculated from the difference between the half-wave and the quarter-wave points with no further illustrated physical relations [42]. SiO_2 films were deposited on sapphire substrates. The authors give exemplary transmission spectra and observe a shift of the short wavelength cut-off toward shorter wavelength with increasing oxygen content. XPS was used for the determination of the stoichiometry of the films, but the results are not given. The transmittance of the films in the spectra is approximately 90 %, which is very poor, but the film thicknesses are not given. Spectroscopic ellipsometry was used to further investigate the films with a VASE instrument over the spectral range of 300–800 nm. With this method, the film thicknesses were also obtained, but not specified. This method is described as a mathematical procedure, which uses regression analysis to minimize the error between the measured data and a model constructed by the known spectral properties of a similar material utilizing Fresnel relations and effective medium theory. The refractive index and the extinction coefficient of SiO_2, $SiO_{X<2}$, and SiO are presented as a function of wavelength.

A spectrophotometer was also used in [43] on AlO_XN_Y films deposited on slide glass. The reflectance at normal incidence was measured in the wavelength range of 400–800 nm. The accuracy was within ±0.1 % and the refractive index increased with increasing AlN content in a concave curved correlation from 1.67 at 0 mol% AlN to 1.73 at 80 mol% AlN.

The optical properties of AlO_XN_Y films are also the topic of [44]. The extinction coefficient, the refractive index, and the film thickness of the films were deduced from spectrophotometric transmittance measurements. The films were deposited on fused quartz substrates, of which the refractive index was also obtained by the transmittance measurements. The system was weakly absorbing, and the mathematical equations used for the evaluation of the resulting spectra consisting of a series of maxima and minima were described in detail. Briefly, the authors interpret the wavelength of the extreme values of the transmittance spectra and the envelope curves of the measured interference spectra in order to gain the refractive index and the absorption coefficient of the films vs. wavelength. In addition to Al_2O_3 and AlN, a film with a composition quoted as $(Al_2O_3)_{0.66}(AlN)_{0.33}$ was investigated and a decrease in the refractive index from 2.08 over 1.808 to 1.666 (at $\lambda > 400$ nm) was observed with increasing oxygen content. Altogether, 11 oxynitride films were evaluated. The dispersion and the absorption edge also shift slightly to lower wavelengths. The composition was evaluated by high-frequency dielectric constant evaluation, and a rectilinear correlation between the refractive index and the oxygen concentration in at% was found. For all films, the absorption coefficient at wavelengths >600 nm was equal to zero ($<10^{-3}$). The energy gap vs. composition is also given. The same group investigated transmission measurements of AlO_XN_Y films in the spectral range of 180–3500 nm [45]. The films were about 250 nm thick, and the optical parameters were determined with this method with an error of ±0.001 for the refractive index, ±0.0005 for the absorption coefficient, and ±2 nm for the thickness. FTIR was used for the analysis of the sample composition. The authors find a critical composition value of 30 % AlN and 70 % Al_2O_3. Below and above this composition, the optical properties of the oxynitride films are similar to Al_2O_3 and AlN, respectively.

Transmittance and reflectance measurements of AlO_XN_Y films deposited on fused silica substrates were carried out in a dual beam spectrophotometer in the wavelength range of 200–2000 nm in [46]. The RBS measurements performed are described in Section 6.1. The transmittance increased when the films approached stoichiometry, but all films showed absorption for wavelengths shorter than 500 nm. The AlN films were nonabsorbing at wavelengths higher than 1000 nm, and this spectral region was used to perform the quarter-wave transmittance calculations for the determination of the refractive index. Since the dispersion curve of AlN was flat over this wavelength range, the values calculated at different wavelengths were still comparable. The refractive index of AlO_XN_Y should span from 1.65 to 1.9 in the visible range of the spectra. The same group of authors investigated AlO_XN_Y in [47] by the envelope method, which is applicable also for weakly absorbing films, and derived the refractive index and the extinction coefficient at 350 and 550 nm. The films showed good transmittance in the near UV and visible with a cut-off wavelength of ~190 nm. The refractive index at 550 nm varied with composition from 1.65 to 1.83. A 15-step Rugate filter (a film with sinusoidal curved refractive index vs. depth) was deposited and reflectance and transmittance were measured. The absorption of the filter at peak wavelength was <0.5 %.

AlO_XN_Y was investigated in [48] as a compound with composition-dependent refractive index, and Rugate filters were produced. The authors emphasized the importance of the quality of interfaces since interfacial phenomena such as light scattering between materials with high refractive index differences, adhesion between materials with different surface and strain energies, etc., are critical especially for films which are subjected to extreme environmental conditions. For the Rugate filters, the interfaces were stronger if the transitions were graded. Therefore, materials with tuneable composition were necessary for Rugate filter production, especially AlO_XN_Y films.

In the study performed by our working group, the measurements were performed with a modified Lambda 19 spectrophotometer of Perkin–Elmer in the wavelength range of 300 to 800 nm and a step width of 0.5 nm. The measurements did show extinction coefficients typically in the range of 0.002 up

to a maximum value of 0.02. Thus, for this sensitive technique, the films exhibit absorption that has to be taken into account for proper calculations. A series of about 20 SiO_XN_Y films was measured and evaluated by a special fitting technique described in detail in [37], which was developed especially for slightly absorbing optical films like oxynitrides. For this fitting technique, starting values have to be chosen. Then, the refractive index, the absorption coefficient, and finally the film thickness are fitted automatically.

In opposition to the results published in [19], the absorption of our films, which were close to the stoichiometry of SiO_2 was enhanced, while nitrogen rich films showed low absorption. An explanation can be found in the problems occurring at high oxygen pressures during deposition. The arcing, which could not be avoided for some deposition parameters, led to the introduction of partly silicon rich droplets into the films and thus enhanced the optical absorption of these films. However, the refractive index, as expected, is linearly dependent on the oxygen content of the films as was demonstrated in [31] and [34]. For AlO_XN_Y films, the absorption was even lower and the surfaces of the films were very smooth.

The latest adaptation of this fitting procedure included calculations accounting for the small oxide-rich interface region between silicon and film due to the native SiO_2 layer on the silicon substrate. Different thicknesses of SiO interface layers extending up to 20 nm were selected, but no significant improvement of the fits in comparison to the single-layer system was achieved. The calculation of a mixture of SiO_XN_Y and small silicon particles was abandoned due to the complexity of the necessary considerations.

Again, this technique exhibits difficulties for films that show absorption or inhomogeneous profiles of the refractive index. Then, models have to be built and fitting procedures developed, which always complicate the interpretation of the results. Nonetheless, this method is much more sensitive to small changes in the refractive index and capable of detecting lower absorption values than ellipsometry. A drawback of this method is the restriction to transparent substrates for many fitting methods owing to the evaluation of transmission measurements.

3. RESONANCE METHODS

3.1 Infrared spectrometry

If the oxynitride films are deposited onto infrared-transparent substrates, the simple and fast IR and FTIR methods can deliver interesting results concerning the bonding of the atoms. It is one of the few analytical methods for thin film characterization that does not need vacuum conditions, and an analysis can be performed within minutes. The absorption bands of Si–N, Si–O, and Si–Si vibrations are relatively strong and can be detected at easy to separate wavenumbers. Furthermore, it is a method that allows gathering information about the concentration and bonding partners of hydrogen, an otherwise difficult to analyze elements. Most of the time, silicon wafers are used as substrate material since they are relatively IR transparent, useful also for other analytical methods because of the high purity level, and technologically relevant as substrate material.

Position and structure of the relevant IR absorption bands are the targets of many investigations. The main absorption feature, the stretching vibration of Si–O and Si–N, is of special interest. This absorption peak has two properties which make it most interesting: the position of the peak maximum usually shifts between approximately 1040 cm^{-1} (SiO_2) to approximately 840 cm^{-1} (Si_3N_4) when oxynitride films are observed, and the peak intensity and area are supposed to vary with film thickness, at least for oxide and nitride films, but no proof is given [49,50]. Even in [51], where the film thickness was determined by ellipsometry and profilometry, the data are given, but the authors do not demonstrate the linear correlation. One also has to take into consideration that the Si–O vibration has a higher extinction coefficient than the Si–N vibration. Two separate features around 840 cm^{-1} (Si–N stretching vibration) and 1060 to 1080 cm^{-1} (Si–O stretching vibration) are observed in oxynitride films in only few

publications [20,23,39,52] and the authors conclude that their films are mixtures of Si_3N_4 and SiO_2 on a microscopic scale according to the RMM. However, in [23] no IR spectrum is given and the samples contain only approximately 6 at% oxygen, which is supposed to stem from surface oxidation. Also in [39], the IR spectra of oxynitride films in correlation to the composition of the samples are doubtful, because even films with an oxygen concentration given as approximately 8 at% show a sharp peak at 1040 cm^{-1} (Si–O vibration), but only a tiny feature at 830 cm^{-1} (Si–N vibration). Thus, the two-phase mixture cannot be confirmed by the reader, and even the authors do not exclude other explanations. TEM was used in [49] to decide whether two phases exist in $SiO_XN_YH_Z$ films produced by PECVD that showed two resolved strong absorptions at 867 cm^{-1} (Si–N) and 1023 cm^{-1} (Si–O) in their IR spectra. The TEM measurements could not resolve two different phases. Nevertheless, the authors concluded that they produced a two-phase film with each phase being about 1–3 nm in size according to the lateral resolution of the TEM. Furthermore, the authors derived the refractive index of the film by calculating the weighted mean of the refractive indices of the SiO_2 and the Si_3N_4 phase. As weighting factors, the IR absorption intensities were applied and the result fitted the experimental value.

The rest of the publications can be subdivided into two groups. The first group of authors interprets the main feature in SiO_XN_Y as a composition of the two stretching vibrations Si–N and Si–O, and therefore the film is seen as a mixture of Si_3N_4 and SiO_2 on the microscopic scale. The second group of authors interprets the peak broadening and the shift in the wavenumber of the main absorption band as the proof for a mixture of Si, O, and N on an atomic scale. The assignment of vibrations to wave numbers in several publications is summarized in Table 1 together with the references. Regardless of the interpretation of the structural background of the main IR absorption band of SiO_XN_Y films, many authors tried to find correlations between the peak position and the composition of the oxynitride films [10,14,23,53–55], which by most authors is supposed to be rectilinear, between the peak position and the deposition parameters [27,56,57], or between the peak position and the physical properties [6,25,52,58,59]. In most publications, such a correlation is indicated, but not verified due to the low sample number or the lack in cross-checking. The interpretation of peak frequency and peak width is complicated by the influence of other film properties such as density, stress and strain, hydrogen bonds, substoichiometry, or defects [23,53,55]. In some publications, the concentration of hydrogen is estimated by the absorption band intensity of hydrogen-related vibration bands [58,60–63] and is even given in the unit atoms/cm^3 in [32]. The detection limit for hydrogen is estimated with 0.5–1.0 at% by a group of authors [10,53,64].

Table 1 Wavenumbers of IR absorption bands collected from various publications.

Wavenumber/cm^{-1}	Description of corresponding vibration	Source
~440	Si–O in SiO_2	[68]
445	Rocking out of plane of Si–O–Si in $SiO_{1.5}N_{0.14}H_{0.14}$	[53]
450	Si atom breathing mode in $Si_3N_4H_{1.2}$	[53]
~450	Rocking vibration in SiO_2	[53]
450	Deformation mode in SiO_2	[6]
460	Si–N in Si_3N_4	[23]
460	Si–O rocking mixed with Si–N breathing	[53]
460	Rocking mode of Si–O–Si in SiO_2, out of plane	[10,58]
469	Si–O in silicon nitride and SiO_XN_Y	[11]
470	Si breathing mode in Si_3N_4	[53]
~475	Si breathing mode in Si_3N_4	[10]
470	Wagging mode of Si–N in Si_3N_4	[25]
~600	Silicon substrate	[68]
~650	Si–H vibration predicted in Si_3N_4	[23]
800	Bending mode of Si–O–Si in SiO_2	[57,58]

(*continues on next page*)

Table 1 (*Continued*).

Wavenumber/cm^{-1}	Description of corresponding vibration	Source
800	Si–O stretching	[6]
~800	Si–H vibration predicted in Si_3N_4	[23]
810	Bending in plane of Si–O–Si in $SiO_{1.5}N_{0.14}H_{0.14}$	[53]
810	Bending vibration in plane in SiO_2	[10,53]
810	Si–O bending mode in SiO_XN_Y	[53]
820	Si–O bending mode in $SiO_XN_YH_Z$ near SiO_2	[71]
~825	Si–O in SiO_2	[68]
830	Si–N stretching mode in $Si_3N_4H_{1.2}$	[53]
830	Stretching vibration of Si–N in amorphous Si_3N_4	[23]
830	Si–N stretching in Si_3N_4	[27,52]
835	Stretching vibration of Si–N in Si_3N_4	[10,53,56,58]
840	Si–N stretching in Si_3N_4	[11,23,25]
860	Si–N stretching in Si_3N_4	[62]
860	Si–N stretching in Si_3N_4 with incorporated H	[23]
870	Si–H bending vibration in $SiO_{1.5}N_{0.14}H_{0.14}$	[53]
~875	Si_2O_3	[74]
890	Si–N stretching in SiO_XN_Y	[75]
~900	Si–N in SiO_XN_Y	[11,57]
~900	Si–N in $SiO_{0.25}N_{1.52}$	[68]
~950	$SiO_{1.47}N_{0.54}$	[68]
980	O/Si ≈ 1	[55]
1040	Stretching motion in plane of Si–O–Si in $SiO_{1.5}N_{0.14}H_{0.14}$	[53]
1040	Si–O stretching mode in SiO_2	[27]
1046	Si–O stretching in SiO_2	[62,63]
1045	Si–O stretching mode in SiO_XN_Y near SiO_2	[71]
1060	Si–O, thickness > 10 nm	[23,49]
1065	Stretching vibration of Si–O in SiO_2	[56]
1070	Stretching vibration in SiO_2	[50,53]
~1075	In plane asymmetric stretching of O in SiO_2	[10]
1080	SiO_2, Si–O in SiO_2, anti symmetric stretching	[25,52,55,57]
1080	Si–O wagging in SiO_2	[6,68]
1130	Si–O in Si_3N_4	[11]
1146	Si–O in SiO_XN_Y (in at%: 35 Si, 19 O, 32 N, 15 H)	[11]
1150	Si–O	[23]
1170	N–H bending in Si_3N_4, also in H-free SiO_2 and in SiO_XN_Y	[23,62,75]
1175	N–H bending in Si_3N_4	[10,53]
1180	Wagging mode of N in Si_3N_4	[25]
1200	Bending vibration of Si–N–H in $Si_3N_4H_{1.2}$	[53]
1560	NH_2	[53]
~1600	Si–D	[72]
1700	H-related band in SiO_XN_Y	[23]
2150	Si–H in $Si_3N_4H_{1.2}$	[53]
2150	Si–H in Si_3N_4	[23,53,62]
2160	Si–H	[23,27]
2170	Si–H in Si_3N_4	[62]
2170	Si–H in SiO_XN_Y	[75]
2195	Stretching mode of Si–H in Si_3N_4	[25]
2213	Si–H in silicon nitride (15 at% H)	[11]
2220	Si–H	[53]
2220	Si–H stretching in SiO_XN_Y, O/(O+N) = 0.58; 15 at% H	[72]

(*continues on next page*)

Table 1 (*Continued*).

Wavenumber/cm^{-1}	Description of corresponding vibration	Source
2228	Si–H in SiO_XN_Y (in at%: 35 Si, 19 O, 32 N, 15 H)	[11]
2245	Si–H stretching in $SiO_XN_YH_Z$ with $x < 1.9$	[71]
2250	Si–H stretching vibration in $SiO_{1.5}N_{0.14}H_{0.14}$	[53]
2260	Si–H	[57]
~2500	N–D vibration	[72]
~2830	H related band in SiO_XN_Y	[23]
3300	Stretching mode of N–H in Si_3N_4	[25]
3320	N–H	[23]
3325	N–H in silicon nitride (15 at% H)	[11]
3330	N–H	[23,27]
3335	N–H stretching in Si_3N_4	[10,51,53]
3340	N–H stretching in Si_3N_4	[62]
3345	N–H	[75]
3350	Stretching vibration of Si–N–H in $Si_3N_4H_{1.2}$	[53]
3350	Si–O–H	[53]
3350	N–H stretching in Si_3N_4	[62,76]
3360	N–H	[53]
3363	N–H in SiO_XN_Y (in at%: 35 Si, 19 O, 32 N, 15 H)	[11]
3370	N–H in $SiO_XN_YH_Z$ near SiO_2	[71]
3380	N–H stretching in SiO_XN_Y, O/(O+N) = 0.58; 15 at% H	[72]
3400	Stretching motion of hydrogen in Si–N–H	[53]
~3450	Si–OH	[8]
3600	Si–OH	[57]
3650	Stretching motion of hydrogen in Si–O–H	[53]
3660	O–H	[53,71]

In structures like $SiO_XN_YH_Z$ or $AlO_XN_YH_Z$ films deposited on silicon, Fresnel interferences are observed in transmission IR measurements and have to be eliminated either by calculation or appropriate measurement conditions [53,61].

IR has been utilized for the comparison of films deposited by different deposition techniques [65]. In this publication, the films deposited by LPCVD showed a broad band as a combination of overlapping bands with various small maxima resulting from the Si–O and Si–N vibrations in the possible N–Si–O bonding environments, while the PECVD spectra showed wider absorption bands with less distinguishable Si–O and Si–N bands because of the more random bonding structure and the higher concentration of hydrogen. The film thicknesses were measured by ellipsometry and step profilometry. For IR analysis, 200–500-nm-thick films were used.

A comparison between ATR and IR reflectance spectra is given in [66]. The composition of the films was determined by AES with an electron energy of 2 keV, using calibration with a SiO_2 and a Si_3N_4 standard produced by another deposition method. The in-depth homogeneity was confirmed by XPS. The film thickness was determined by ellipsometry. The reflectance of the films was measured with a Perkin–Elmer 983 double-beam spectrophotometer in the range of 200–2000 cm^{-1} at an angle of incidence of 45°. The ATR experiments were performed on a Perkin–Elmer 1760X FTIR spectrophotometer with unpolarized light at 45° incidence and a KRS-5 crystal. IR and ATR spectra were also utilized by the authors for the evaluation of films for passive radiative cooling applications, because in this case for the multilayered designs the depth resolution was not necessary, only the overall reflectance was of importance [67].

Spectral transmittance and reflectance were measured in [68] in the wave number range of 200–2000 cm^{-1} with a Perkin–Elmer 580B double beam spectrophotometer equipped with a variable-

angle reflectance attachment, a polarizer, and an air dryer. Freshly evaporated Au mirrors were applied as reflectance standards. The films investigated in transmission were backed by silicon, the films investigated in reflectance by aluminum-coated glass. The composition was determined by RBS. The possible normal vibrations of tetrahedral molecules are discussed. The authors state that out of nine vibrations, six are infrared active, and when calculating the vibrations for mixed tetrahedra with nitrogen and oxygen, the different atomic masses remove the symmetry. With these calculations, an almost linear variation of the resonance frequencies with composition is suggested. The effective medium theory with the assumption of a two-component mixture of SiO_2 and Si_3N_4 and mixing on an atomic scale with the five possible tetrahedra formed by silicon surrounded by oxygen and/or nitrogen according to the RBM were investigated. The conclusions are that a two-component mixture of oxide and nitride cannot describe the observed data and the assignation of the monotonic shift in the main absorption frequency as a function of composition to the mixed crystal theory. The agreement between the experiment and the calculated complex dielectric functions was satisfactory for the authors.

IRRAS measurements of silicon oxynitride films with thicknesses lower than 50 nm were performed in [69]. The authors wanted to take advantage of the different behavior of *s*- and *p*-polarized light in dependence of the angle of incidence. The films were also characterized for their refractive index and thickness by a SOPRA UV–vis spectroscopic ellipsometer. The reflectance spectra of the films dependent on the different substrate types were compared. The IR spectra were recorded with an FTIR instrument of Nicolet at 4 cm^{-1} resolution. The angle of incidence was either 70° or 80° from the normal to the surface. Either the ratio of reflectance for *p*-polarized incident light to *s*-polarized light or the ratio of the *p*-polarized signal without film to the signal with film was measured. The authors found a linear dependence of the longitudinal optical mode of the Si–O band on the film refractive index, but also on the film thickness. It is not quite clear why the authors normalized the refractive index by division with the film thickness. Thus, film composition can be determined by IRRAS as long as the film thickness is known and quantified reference samples are available.

Film thickness and refractive index of thermally grown silicon nitride films, which turned out to contain a fairly high amount of oxygen, were determined by ellipsometry in [70] without further specification of the instrument used. The authors combined this method with AES, electron diffraction, and IR. They observed IR absorption peaks at 893 and 848 cm^{-1} and associated the latter feature with the Si–N stretching vibration of crystalline films, since this feature increased with increasing crystalline size. The position of the peak at 893 cm^{-1} was used to estimate the composition of the film. Water vapor and oxygen in the residual gas were blamed as sources for the local crystallization of the films by vapor etching.

Quantitative IR analysis was attempted by [71]. ERDA was used for the quantification of silicon, oxygen, nitrogen, and hydrogen in the standard samples. The measured spectra of overlapping features were deconvoluted, and the fitted Gaussian bands were evaluated. For films near SiO_2, the IR absorption maxima are specified in Table 1. For $SiO_XN_YH_Z$ with $x < 1.4$, a large Si–H stretching was observed consisting of two bands at 2240 cm^{-1} decreasing to 2200 cm^{-1} and 2150 cm^{-1} decreasing to 2110 cm^{-1} with decreasing x. For $x < 1.6$, a large mixed band was observed between 750 and 1100 cm^{-1}. Three sub-bands were necessary to fit this feature, a Si–O bending at 820 cm^{-1} decreasing to 780 cm^{-1}, a Si–N stretching at 850 cm^{-1}, and a Si–O stretching at 1045 cm^{-1} decreasing to 1010 cm^{-1} with decreasing x. For samples with $x < 1.5$, the authors, therefore, postulate two separated insulating phases $SiO_{X'}H_{Y'}$ and $SiN_{X'}H_{Z'}$. The hydrogen concentration was calculated from the intensities of the IR absorption bands and the oscillator strength with an accuracy compared to ERDA of ±50 %. No correlation between the intensity of the absorption bands and the contents of Si–O or Si–N was found, but linear correlations between the Si–O and Si–N wavelength and the concentration were calculated with an accuracy of ±9 % for oxygen and ±25 % for nitrogen.

A rather uncommon application of IR is the differentiation between hydrogen and deuterium [72]. The samples were annealed in a deuterium/nitrogen atmosphere in order to investigate the diffusion processes.

Multiple internal reflection IR spectrometry was employed in [73] to determine the chemical bonding of hydrogen.

The interpretation of IR spectra is not always conclusive. As can easily be derived from Table 1, the interpretation of the origin of features at one and the same wavelength varies widely from publication to publication. Attempting to interpret each smallest little bump also can lead to inconsistencies such as in [11], where a Si–O vibration feature was described in a Si_3N_4 film, which, according to RBS, contained oxygen in a concentration <0.1 at%.

The IR spectra of amorphous AlO_XN_Y films were shown in [43] in the spectral range of 450–1200 cm^{-1} together with a spectrum of crystalline hexagonal AlN powder. Broad absorption bands from 500–900 cm^{-1} were observed in all films. The spectrum of amorphous Al_2O_3 showed two close maxima at approximately 600 and 800 cm^{-1}, while AlN had one maximum at approximately 700 cm^{-1}, which was assigned to a stretching vibration. With increasing AlN content, the feature at 600 cm^{-1} representing AlO_6 octahedra became smaller and disappeared for compositions >50 mol% AlN, while the feature at 800 cm^{-1} representing the AlO_4 tetrahedra remained unchanged until 50 mol% AlN and then decreased in intensity. The 700 cm^{-1} feature increased with increasing AlN content.

IR spectra of AlO_XN_Y were also determined in [44,45] in the spectral range of 400–4400 cm^{-1} and the observed feature at 460 cm^{-1} was identified as a vibrational mode of the Al_2O_3 molecule, the peaks at ~680 cm^{-1} (strong) and 1180 cm^{-1} (weak) were identified as AlN vibrational bands. Other publications were cited with slightly deviating values for the AlN absorption feature of 1057, 714, 700, and 675 cm^{-1}. Peaks at ~3450 and 1640 cm^{-1} were assigned to OH bands.

Other than the above publications on AlO_XN_Y films, in [47] no absorption lines of Al_2O_3 and AlN were observed by FTIR, the authors in fact could not find any special AlO_XN_Y absorption peak.

A theoretical interpretation of the IR properties of AlO_XN_Y films by the aluminum-centered tetrahedral model was tried in [77]. The material was considered a mixture of two species for the calculation. Surprisingly, the RBM was applied and the composition of the tetrahedra is attributed to the volume fractions of Al–O and Al–N; AlO_4, AlO_3N, AlO_2N_2, $AlON_3$, and AlN_4 tetrahedra were considered. Spectra were measured in the 400–4000 cm^{-1} range by an FTIR spectrometer and compared to the modeled curves according to the RBM. The authors observed a decrease in the amplitude and a 30 cm^{-1} shift of the transmittance minimum to lower wavenumbers with increasing oxygen content. The precision of the spectrometer was 4 cm^{-1}. The composition was determined by XPS measurements after sputter cleaning of the surface with a 4 kV, 50 µA ion beam.

IRRAS measurements of AlO_XN_Y films with thicknesses in the range of 1 nm were performed in [78] with a resolution of 8 cm^{-1} with polarized radiation, which enhances the effects of the adsorbates. In this case, mainly chemisorbed NH_3 was investigated.

AlON powders were investigated in [79]. XRD, FTIR, and ^{27}Al NMR were used, but no quantification was performed.

All FTIR transmission measurements of our working group were performed on a Shimadzu FTIR-8201 PC with a resolution of 4 cm^{-1} in the range of 4000–350 cm^{-1}. For each spectrum, 200 scans were performed. The layout of a typical FTIR instrument similar to the one applied in this work is given in [80]. The substrate of the oxynitride films has to be IR transparent, consequently, silicon substrates were used.

FTIR results are summarized in [81] and compared to other applied analytical techniques. The silicon substrates were IR transparent, but the samples nevertheless showed strong absorption due to their thickness. An additional effect was observed, which now is being investigated by other groups [82]: obviously, the IR radiation transmitted through the complex of the deposited film and the silicon wafer is subjected to interference effects, which cause strong oscillations of the observed intensity if the adjustment of the resolution of the instrument is high enough [61]. Since this effect was not of interest in our study and such a high resolution was not needed due to the relatively broad absorption features, the resolution of the instrument was set to a value of 4 cm^{-1}, thus avoiding difficulties in the evaluation of the spectra used in [87].

With the IR measurements performed on oxynitride films, some of the assumptions made in the literature were confirmed in [81]. All investigated SiO_XN_Y films did show one broad absorption feature in the wavenumber range between the absorption peak of SiO_2 and Si_3N_4. In [81], a linear correlation between the area of the absorption feature and the film thickness was established. The position of the absorption maximum was evaluated for all films and a linear correlation between the sample composition and the wavelength of the absorption maximum was found. Consequently, IR analysis can be used for a fast estimate on film thickness and composition. This result also leads to the conclusion that the SiO_XN_Y deposited by reactive dc-magnetron sputtering is not a two-phase mixture of SiO_2 and Si_3N_4, but a material composed of mixed N–Si–O tetrahedra [83].

For AlO_XN_Y films, a broad absorption feature with two maxima was observed for the Al_2O_3 film and a sharper feature at an intermediate position for the AlN film, also described in detail in [81]. In this case, the resulting AlO_XN_Y spectra were superpositions of the oxide and nitride spectra. With peak deconvolution, the contributions of the oxide feature and the nitride feature to the resulting oxynitride spectra were calculated. An example is given in [84]. A linear correlation between the peak area of the Al–N feature and the composition was found. The results given in [81] partly fit with the results of [43]. The area of the oxynitride absorption feature also was proportional to the film thickness. Nonetheless, the atomic structure of the AlO_XN_Y films seems to be different from the SiO_XN_Y films.

Since some authors stated exceptionally low limits of determination for hydrogen of 0.5–1 at%, the FTIR measurements were also evaluated with respect to hydrogen absorption features. NRA data of hydrogen were applied for the quantification. The published data could not be verified—the limit of detection for hydrogen was higher than 2–3 at% and the limit of determination higher than 10 at%.

In summary, FTIR is a fast and reliable tool for the survey of the composition of silicon oxynitride films and of the film thickness of SiO_XN_Y and AlO_XN_Y films, whereas the determination of the composition of aluminum oxynitride films is limited by the deconvolution procedure to higher concentrations of oxygen and nitrogen.

3.2 Raman scattering

Raman scattering with an argon laser at 514.5 nm and 300 mW was measured with a Jobin Yvon Spex T64000 TA-S spectrometer in [85]. The Raman shift of the silicon oxynitride films was observed in the range of 250 to 650 cm^{-1}. After annealing of the silicon-rich films, silicon clusters resulted in a signal at ~500 cm^{-1}. The films were also analyzed by XPS.

3.3 Electron spin resonance

Electron spin density measurements for unpaired electrons in [65] showed that films with a refractive index of 1.75–1.78 had the lowest spin density. The films were 1–2 μm thick and deposited on silicon substrates. The measurements were performed at room temperature and at liquid He temperature and compared to standardized CVD Si_3N_4 material. The detection limit of this system was 10^{11} spin/cm^3. The ESR signals observed were attributed mainly to silicon and to a small extent to nitrogen dangling bonds. The authors then discussed the possible N_2–Si–O_2 structure as the reason for lower stress, higher thermal stability, and lower pinhole density of films with a refractive index of 1.75–1.78.

ESR measurements were performed in [38] at room temperature and normal pressure. The spin density measurements were performed at a modulation frequency of 100 kHz at low power. For SiO_XN_Y films, a decrease of the so-called *g* value (a dimensionless constant and a physical property of the electron) with an increase of the oxygen content in the films was observed. Various ESR spectra were given and the defects causing the effects in ESR were examined for SiO_XN_Y films. ESR measurements were used to evaluate the number and kind of defects.

3.4 Photoluminescence

Photoluminescence properties of silicon oxynitride films were investigated in [86]. The composition of the films and the film thickness were controlled by single wavelength ellipsometry, and RBS was used for calibration. FTIR measurements with a resolution of 4 cm^{-1} and reflectance and transmittance measurements were recorded. The PL measurements were performed with the 488-nm line of an argon laser and the 325-nm line of a HeCd laser. A double grating spectrometer with a GaAs photomultiplier was used. The dependence of the PL on temperature was evaluated with a Joule–Thompson refrigerator at 77 and 300 K. Electron paramagnetic resonance spectra showed five lines and a total paramagnetic defect density of 2×10^{19} cm^{-3}, which can be reduced by annealing. Stoichiometric samples show only one line. High refractive index films did not show any photoluminescence at room temperature. At the higher laser wavelength, the film with a refractive index of 1.6 showed photoluminescence at 2.21 eV, which increased to 2.3 eV as the refractive index reached 1.65, and decreased again to 1.71 eV as the refractive index increased to 2.7. Annealing at a temperature of 950 °C caused a red-shift of 0.05 eV. The photoluminescence energy at the lower laser energy is 2.8 eV at a refractive index of 1.65 and decreased to 2.1 eV for a refractive index of 2.1. After annealing at 950 °C, the red-shift is 0.15 eV. The effect of the annealing on the photoluminescence intensity was also investigated. The authors concluded that the photoluminescence can be explained by tail-state luminescence, but also by defects. The active centers of the near-stoichiometric films are supposed to be Si–Si bonds or Si–H bonds near voids. The lifetime of the photoluminescence is in the range of 10 ns.

4. X-RAY ANALYTICAL TECHNIQUES

4.1 X-ray photoelectron spectrometry

Next to AES, this method is one of the most commonly applied surface analytical techniques, although the spatial resolution is worse than for AES. The sample is bombarded by X-rays, which cause the emission of inner-shell electrons of the bombarded atoms. The kinetic energy of these electrons is measured. The energy of the photoelectrons results from the energy of the exciting X-ray beam minus the binding energy of the electron, which in turn depends on the excited atomic species. The accuracy of quantitative analysis is limited. For insulating samples, charging effects can be a problem. When combined with argon ion sputtering, depth profiles can also be obtained with this method. Furthermore, this method is sensitive to the chemical surroundings of the element under investigation since the peak position varies slightly depending on the bonding partners.

In [87], the investigations were carried out with Al Kα excitation and Ar bombardment by a Penning discharge ion gun. Si 2p, O 1s, and N 1s were quantified for depth profiling. The resulting Gaussian Si 2p peaks were recorded after each ion bombardment step and deconvoluted afterwards. In the deconvolution calculations, all possible tetrahedral configurations of the Si atoms were included, ranging from elemental silicon to silicon atoms being surrounded by four oxygen and/or nitrogen atoms. Since the observed samples in this case were prepared by ion bombardment of silicon, intensity changes of several oxidation states (configurations) of silicon were observed during depth profiling. With these results, the authors explained the formation of dangling bonds and therefore trapping centers in the samples. They obtained SiO_XN_Y, which they described according to the deconvolution as a chemically ordered atomic mixture of Si bonded to O and N following the RBM.

Growth mechanisms of films have also been investigated with XPS. Oxynitridation of Si was used for thin film deposition and the Si 2p peak was examined at progressive in situ Ar ion milling in [88]. In the middle of the film, the Si 2p peak maximum shifted to lower binding energy and this new feature was deconvoluted. While the surface of the film was SiO_2, in this depth Si_2N_2O was reported as the main composition, then the interface to the silicon substrate was reached. The authors concluded that at the beginning, SiO_2 was formed and that nitrogen diffused through the oxide and reacted at the

interface to form the oxynitride. The higher affinity of oxygen to silicon in comparison to nitrogen was shown.

High-resolution spectra were obtained in [89] for the Si 2p, C 1s, N 1s, and O 1s features using a magnesium anode as the X-ray source. The chemical composition was calculated from the integrated peak intensities. Sample charging was accounted for by referencing the peak energies to the C 1s photoelectron peak. The Si 2p peak position was used to study the local chemical environment in SiO_XN_Y films. Pauling analysis (based on the Pauling charge model) was applied to explain trends in photoelectron binding energy shifts based on compositional changes. The rectilinear decrease in the Si 2p binding energy with increasing nitrogen content was confirmed. Si_3N_4, SiO_2, and Si_2N_2O reference materials were used without further specification to describe the dependence of the Si 2p binding energy by the structural subunits with Si tetrahedrally bonded to four oxygen atoms, four nitrogen atoms, and one oxygen and three nitrogen atoms, as nitrogen replaces oxygen in the tetrahedra. A linear dependence between the average charge of the Si atoms in SiO_XN_Y calculated by the model and the observed Si 2p binding energy was shown. This model should even cover the Si 2p binding energy of silicon-rich films.

The C ls line of carbon was also used as a reference line in [62,63]. The XPS spectra were recorded with a VG Escalab MKII, VG Scientific, using a Mg Kα source with an energy of 1253.6 eV at a pressure of 1.3×10^{-6} Pa. A slight shift of all lines was observed due to sample charging, and, therefore, the carbon peak stemming from the residual carbon at the surface was used as reference. The binding energies of Si 2p, N 1s, and O 1s electrons and the FWHM were derived from high-resolution spectra using pass energies of 25 eV. With increasing nitrogen content, a continuous decrease of the binding energy was observed resulting from the decrease in electronegativity. UV/VIS spectrometry was used to determine the optical band gap of the films in the range of 190–550 nm.

Also in [38], the relative bulk concentrations x and y of oxygen and nitrogen in SiO_XN_Y were determined by measuring the O 1s, Si 2s, and N 1s line areas utilizing a Mg Kα source. In order to assure the in-depth homogeneity, the sample surface was Ar-ion etched. The drawback of this procedure, preferential sputtering, was recognized, since the direct determination of the composition utilizing photoelectric cross-sections and correction factors yielded much too low oxygen and nitrogen contents. Only the direct comparison of the peak areas with those of standard SiO_2 and Si_3N_4 samples yielded useful results. The comparison of the sample spectra with the standard spectra did not show a superposition of Si, SiO_2, and Si_3N_4 spectra in the partly substoichiometric films, therefore the formation of Si–N and Si–O bonds on an atomic scale was deduced. Also, in this case, no informative details about the standards used or the sample charging effects were given.

XPS measurements on SiO_XN_Y films with a PHI 5701 LSci instrument with a monochromatic Al source and a concentric hemispherical analyzer were performed in [90]. Charge neutralization was achieved by a low-energy electron flood gun, but nonetheless, the peaks were charge referenced to the Si 2p peak of a SiO_2 band. The take-off angle was 65° with respect to the sample surface. Relative sensitivity factors were obtained by the measurement of two polymer standards. SIMS measurements on a Phi quadrupole instrument were performed with Cs^+ sputtering at 1 keV, and the cesium molecular ions were detected in order to determine the depth distribution. NRA measurements were performed with the reaction $^{14}N(d,\alpha_{0+1})^{12}C$ at 1.1 MeV to check the results. The N 1s peak is inspected carefully for coordination with Si, O, and H, under consideration of next-neighbor effects. The authors state that quantification of the films with thickness values lower than 6 nm proves difficult and is possible only if several assumptions are correct, the most important being a homogeneous depth distribution. At least in this publication, the necessary calibration procedures are described in detail and an explanation for the results differing from the NRA results is given and explained with the inhomogeneous depth profiles.

The long-term stability of SiO_XN_Y films with a thickness of about 100 nm on solar cells was investigated in [91]. No information about the measurement procedure was given. Only intensity vs. etching depth profiles were displayed without giving details about the way the sample was etched or the

way the etching depth was determined. The interpretation of such spectra is, therefore, questionable. Reflectance curves for the antireflective coatings were given, and the refractive index was found to be directly proportional to the film density.

Even more doubtful are depth profiles when essential facts typical for all sputtering processes, like the Ar ion sputter rate, sputter yields, and preferential sputtering, are neglected, because only the qualitative depth distribution is of interest. In such cases, at least no atomic concentration should be specified [67]. Only depth profiles of the heat mirrors for passive radiative cooling were recorded with XPS, the composition was determined by either AES or RBS with SiO_2 and Si_3N_4 films as standards, which were produced by other deposition methods.

Usually XPS is just mentioned as the analytical method utilized for the determination of the composition or just for the comparison of samples [92,93]. Since the quantification seems to be straightforward, many authors do not give information on the problems they encountered or on the accuracy of the results. An example for this practice is [23], where the information was limited to the rudimentary data. A Physical Electronics model 560 spectrometer with a background pressure of less than 6.7×10^{-7} Pa was applied and standard atomic sensitivity factors and instrumental corrections associated with the instrument were used. Part of the sample was coated with gold in order to provide a binding energy reference. The photoelectron energies were corrected with respect to the Au $4f_{1/2}$ line at 83.8 eV and an oxidized surface of approximately 10 nm thickness was found.

The chemical bonding of AlO_XN_Y films was determined with a Perkin–Elmer PHI 5100 system with Mg Kα radiation [47]. The films were sputter-cleaned at 70° with argon ions at 4 keV. Films with x varying from 0.84 to 1.52 and y varying from 0 to 0.60 were produced. The Al 2p, O 1s, and N 1s peak were observed in order to decide, whether the films were mixtures of the kind described by $(Al_2O_3)_{1-C}(AlN)_C$, or a compound of the AlO_XN_Y type. In a mixture, the Al 2p peak was supposed to be a doublet, in the other case, a single peak should have been visible. The authors observed a single peak with a binding energy shifting due to compositional changes. Also the oxygen and nitrogen peaks behaved similarly, and, therefore, AlO_XN_Y was defined as a compound. Spectra are shown and the peak position and the emerging of a new nitrogen peak are discussed in detail. The films were amorphous according to X-ray diffraction analysis.

In [94], the take-off angle of the Quantum 2000 ESCA microprobe XPS instrument was set to 20° to increase the depth resolution, which the authors claim to be in the same range as the TOF–SIMS depth profile. 500 V argon ions were used for sputtering. Shifts in binding energy were attributed to differences in chemical, mixtures of chemical states were observed as multiple peaks and broad peaks.

Silicon oxynitride films were prepared on silicon wafers in [95] and characterized by XPS with a Cameca Riber Sia 250 device. Argon sputtering was applied with 3 keV, and charging effects were observed. Thus, the carbon peak due to contamination was used as reference, and the Auger parameter was applied. The areas of the Si2p, O1s, and N1s lines were evaluated. The Si(KLL) Auger line was excited by the Bremsstrahlung from the Al anode. FTIR transmission measurements were performed with a Nicolet 4000 instrument. IR was used for the determination of the hydrogen concentration, which was in the range of 5 to 30 at%, depending on the film composition. The same group of authors published XPS, AES, and FTIR measurements in [96]. In this publication, slightly different instrumental parameters were chosen by the authors with an argon beam of 4 keV and a filtered Al source with a beam energy of 12 keV. The area of the core-level signals is evaluated for the determination of the film composition. The samples were analyzed by ellipsometry and several models for the interpretation of the refractive index are discussed. The authors interpret the films as a phase mixture of silicon and oxynitride or SiO_XH and SiN_YH. The refractive index varied between 1.45 and 1.8.

XPS analysis of silicon oxynitride films was performed in [75] with an LHS-10 spectrometer utilizing the Al source with 13 keV at 20 nA. The authors used a pure silicon nitride powder from Aldrich (≥99.9 %) as reference material. O 1s, N 1s, Si 2p, and Si(KLL) were observed. The C 1s signal stemming from surface contaminants was used as the reference signal. The powder did not contain carbon, thus the N 1s line was utilized. A list of XPS results of publications by other authors is included. All

samples, including the reference “silicon nitride” powder, contained oxygen. The authors found approximately 90 % silicon nitride phase and 10 % silicon oxynitride phase in the commercial powder. The composition of films and powder was not investigated.

4.2 X-ray excited Auger electron spectrometry

In a very comprehensive publication [97], the authors describe the advantages of XPS over AES for the analysis of SiO_XN_Y films as immense, especially if information on the coordination of the atoms is wanted. The beam damage is avoided and chemical shifts, line broadening, and fine structure are easier to study. In their opinion, even the quantification is straightforward. Consequently, XAES was applied in this publication. A VG ESCALAB 2 spectrometer was applied and unfiltered Al Kα radiation was used for the excitation. An energy resolution of ~1.1 eV utilized at a source power of 300 W. For the quantitative depth profiles, a Leybold–Heraeus IQE ion gun was used, working at 0.5–4 keV while being rastered over an area of 8×8 mm^2 with a spot size of 0.5 mm, but only an area of ~5 mm diameter was analyzed. The films had a thickness of 15–100 nm. Relative sensitivity factors for O and N were determined from not specified thin film oxide and nitride standards prepared by coworkers, and their stoichiometry was checked by ERDA only. Peak shifts due to the still present sample charging were corrected by the use of the Auger parameter as the observed quantity, which in simplified form is the difference between the positions of two peaks in the same spectrum. The results of the quantification of SiO_XN_Y films by XPS and Ar sputtering showed a general systematic deviation from the RBS/ERDA results of 4.5 %, but the values were approximately 13 % lower than the nominal value. An exact description of the obtained spectra followed, but the generally more interesting result was the fact that the Auger parameter varied monotonically but not linearly with the determined composition from SiO_2 to Si_3N_4. Out of this observation and defining the valences of oxygen as 2 and of nitrogen as 3, the theoretical values for the Auger parameter for the intermediate configurations with the tetrahedra SiO_3N, SiO_2N_2, and $SiON_3$ were calculated and these values indeed had a bow-shaped form, but the measured values had an even stronger curvature. This effect was attributed to the enhanced influence of nitrogen on the silicon relaxation energy in comparison to oxygen and was further investigated. The conclusion was that the Si (LVV) peak was not suitable for quantification. During Ar ion bombardment in the energy range of 0.5–4.0 keV, only the first atomic layer was damaged, but this influence was avoided by using the high kinetic energy Si 2s and 2p and the Si(KLL) Auger emissions for the Auger parameter and thus compositional and coordination analysis. The results confirmed the RBM.

Also, [98] used X-ray initiated Auger spectra produced by the Bremsstrahlung of the magnesium anode in the XPS system for the characterization of SiO_XN_Y films, and the Si 2p, O 1s, N 1s, $Si(KL_{2.3}L_{2.3})$, O(KLL), N(KLL) peaks, as well as the valence band were investigated. RBS was used for to estimate the bulk composition. The sample charging of the 1.5–2 μm thick films was determined by referencing the O 1s to a certain energy, and, together with given photoionization cross-sections, the spectra were evaluated. The two silicon peaks showed shifts with the change in film composition and the extent of the Auger peak shift was three times the photoelectron peak shift. The N 1s and O(KLL) peaks did not show significant changes with sample composition. Since the peak shape and width of the Si(KLL) peak remained unchanged and only the position varied linearly with composition, it was concluded that N and O were bonded on the same Si atom following the RBM.

4.3 X-ray diffraction

X-ray diffraction was used to analyze the structure of the deposited films in [23], where the rf-sputtered oxynitride films showed the characteristic halos of amorphous films. Also, diffractograms taken in [68] on 2-μm-thick SiO_XN_Y films deposited by reactive rf-magnetron sputtering on Si substrates were featureless and the films defined amorphous. This method was often combined with electron diffraction

[98], and the crystallinity of the films as deposited and after sample treatments such as annealing was investigated.

Also in [99], the crystallinity was tested by XRD at an angle of incidence of 1°. From the absence of signals in the pattern, the samples were described as amorphous. XRD was also used in [100] to analyze the crystal structure of silicon–aluminum–oxynitride films with an RINT 7000 Rigaku Co. instrument, due to the same reason as above the films were supposed to be amorphous. In this publication the film composition was determined by AES and even depth profiles were quantified. Unfortunately, no details on the quantification were given.

The instrument used by our working group was a Siemens D 5000 with Bragg–Brentano geometry, and Cu Kα radiation was used. The analytical parameters for the measurements were a sample rotation speed of 60 revolutions per minute, a time per step of 1–20 s depending on the range of the 2-theta scale that was investigated. For survey, a 2-theta range of 20 to 80° and a step width of 0.03° was chosen.

All SiO_XN_Y films turned out to be X-ray amorphous, but some of the AlO_XN_Y films did show diffraction patterns. Thus, only AlO_XN_Y films were investigated more closely by XRD. The composition of the samples with crystalline reflections was in the range of 5 to 20 at% oxygen. During this series of measurements, the difficulties in the evaluation of the observed spectra were rooted in the thin film character of the investigated samples. The intensities of the peaks under investigation varied from sample to sample not only in general, but also the intensity ratios of various peaks did not remain constant. This effect was observed even for samples with similar composition and is supposed to be a result of crystals with preferred orientation. Nevertheless, the diffraction pattern could clearly be attributed to hexagonal AlN. The pattern used for this comparison was JCP 25-1133 [101]. Furthermore, the position of the XRD-peaks changed slightly for different samples despite the similar composition. Unfortunately, it could not be determined conclusively whether this effect was due to actual changes in the composition of the diffracting crystals or to film stress. The dislocation of the peaks that shifted to higher 2-theta scale is the result of a reduction of the lattice constant *a* of the hexagonal lattice of AlN, which is demonstrated by the original database pattern and the pattern shifted by variation of the lattice constant *a*, and actually might result from the incorporation of oxygen.

Comparative analysis with utilization of a Göbel mirror (parallel beam geometry) did not show any improvement in the quality of the achieved spectra.

4.4 X-ray reflectometry

In [102], monochromatic Cu Kα radiation was used for measurement of the specular reflection curves of amorphous $SiO_XN_YH_Z$ films. The incident-collimated X-ray beam had a nominal angular divergence of 0.01°. The film thickness was determined from the interference fringes of the obtained curves and compared to results obtained by ellipsometry and optical absorption measurements. Furthermore, the density was determined by the critical angle of the total reflection, and surface and interface roughness were evaluated. The precision for the density was given as 5–10 %, for the thickness even better than 3 %. Anyway, the thickness results were 3–9 % higher than those of the ellipsometry measurements but were in good agreement with the optical absorption results. The obtained densities also varied from the ERDA values, because the latter method was probing a deeper sample volume.

Grazing incidence X-ray reflectometry was also used in [96] to determine the density and film thickness. The film thickness was compared to ellipsometry results, but the density was compared only to theoretical values. A Siemens D5000 instrument was used at critical angle.

4.5 Grazing incidence X-ray scattering

In this technique, the incident X-ray beam is totally reflected [102], and since the transmitted wave has an evanescent propagation, the irradiated depth is low and almost no background is observed. The in-

strument used was similar to the X-ray reflectometry instrument, but another detector that allowed a diffraction spectrum to be obtained over the angular range of 120° was used. The measurements were performed near the total external reflection with an incidence angle of 0.3°. The scattering was observed perpendicular to the surface for several SiO_XN_Y samples and SiO_2 and Si_3N_4 films. A linear combination of the oxide and nitride diagrams would have resulted in a sharper diffraction peak than observed and in a shift of the second intensity maximum toward lower scattering vector values. The authors interpreted these observations as a less-ordered network and a lower average distance between first-neighbor pairs in the films in SiO_XN_Y than in SiO_2 and Si_3N_4. Other X-ray techniques were also applied in this paper.

4.6 Grazing emission X-ray fluorescence spectrometry

This method is similar to wavelength-dispersive X-ray fluorescence, but only the radiation emitted under grazing angles is measured [103]. The authors state that the composition of the films, the depth distribution, and the densities of the films can be determined by angle-dependent measurements. The film thickness of the samples produced thermally was in the range of <5 nm. The measurements were performed on a modified Philips XRF spectrometer, and a polychromatic Rh anode was used at 3 kW. The experiments were performed in vacuum at slightly elevated temperature, and the emission angle was 0 to 0.1 rad. The information obtained by the measurements is described generally. The angular dependence of the O Kα and N Kα fluorescence was investigated. The relative error of the oxygen concentration is given as 3 %, according to repeatability measurements. Due to the low net count rates, the authors admit a precision of 20 %. Some samples were compared to AES and RBS results. The correlation to AES was good, but due to the high standard deviation of RBS, the results for nitrogen did not fit well.

4.7 Extended X-ray absorption fine structure

This method of analysis is used relatively rarely because of the need of synchrotron radiation sources. In [104], the X-ray absorption was measured at the Si K edge at ~1840 eV. The current necessary to compensate the sample charging due to the photoelectron emission was measured. According to this publication, the information obtained corresponded to the total absorption coefficient and contained no substrate contribution. Therefore, the composition of the films was extracted from the step heights of the resulting signal by using atomic absorption coefficients. The results were compared to XPS results obtained from core-level peak areas and were consistent within the experimental error given as ±5 %. Further information on the conduction band density of states was obtained from the region of the spectrum near the absorption edge by the XANES. Information on the atomic structure was extracted from the EXAFS itself. This way the bond lengths in SiO_XN_Y were determined, and the values were very similar to the bond lengths in SiO_2 and Si_3N_4. Furthermore, the spectra did prove the amorphous structure of the films, because no higher coordination spheres could be detected. Nevertheless, the stoichiometric films were proven to be chemically ordered with a fourfold-coordinated Si by nitrogen and/or oxygen only, each oxygen atom bonded to two and each nitrogen atom bonded to three silicon atoms.

4.8 X-ray absorption near-edge structure

The XANES measurements in [102] were performed at the French synchrotron radiation facility, and the spectra were collected in the electron yield mode at the Si K edge. Crystalline Si, quartz, Si_3N_4, Si_2N_2O, and amorphous fused silica were used for comparison. Samples with an O/(O+N) ratio of 0 to 1 were studied. The Si K edge energy increased with increasing oxygen due to the electronegativity of

the chemical environment. Linear combinations of crystalline SiO_2 and Si_3N_4 diagrams were very different from the experimental data of the $SiO_XN_YH_Z$ films.

5. ELECTRON BEAM ANALYTICAL TECHNIQUES

5.1 Electron probe microanalysis

EPMA is a widely used analytical method for film characterization concerning metal films or compound films of one inorganic component, as long as film and substrate contain different metals. In the case of silicon and aluminum oxynitride films on silicon substrates, there are two difficulties to be dealt with. First, the resulting X-ray signals of oxygen and nitrogen are very close in the energy spectrum, and, therefore, it is difficult to quantify small amounts of oxygen or nitrogen when a higher amount of the other element is present. Second, the signal generated by the substrate influences the signal generation in the film if the film is thinner than the excitation depth of the method.

In EPMA, there are two fundamental ways of signal detection and processing, WDS and EDS. For a long time, WDS was mostly applied since the technological development was further advanced than EDS. Many investigations and developments on thin film analysis by EPMA were performed by the group of G. F. Bastin. He had to face many problems when analyzing light elements like oxygen and nitrogen by WDS-EPMA. This is due to the fact that the X-ray energies of the characteristic lines are positioned in the region lower than 0.7 keV of the energy spectrum, which allows the effective emission of the generated X-rays to take place only in very shallow depth [105,106]. Another difficulty occurs if the emission energy of the analyzed element coincides with the absorption edge of an accompanying element [107–109], which makes it necessary to reduce surface contamination caused by long analysis times [105,109]. The surface roughness of technological samples complicates the evaluation of the results, since changes of the take-off angle of 5° can alter the results by 10 % when performing the analysis at the relatively shallow take-off angle of 32° [106,108]. When using WDX, with its relatively high resolution in comparison to EDX, it is difficult to cope with shifts in peak position and peak shape alterations, because the emission profiles depend on the chemical bonding in the material and on the crystalline orientation, as is also shown by G. F. Bastin in [105,106,108,110,111]. In order to achieve reliable results, time-consuming integral recording of the peaks is necessary, which stands against the necessity to shorten analysis time in order to minimize contamination of the surface with carbon and, especially in the case of sensitive films, with oxygen [106,108,112]. Due to the use of a crystal to separate the X-rays according to their wavelength, higher-order reflections of the heavier metal fraction in the films [108,110] can cause problems in spectrum evaluation. Utilizing WDX for the analysis of silicon oxynitride films requires a lot of time, and the results are not always very accurate.

Other authors apply EPMA for the determination of the stoichiometry of their silicon oxynitride films, without giving details about the calibration of the instrument [61], whether it was an EDS or WDS [113], but specify the error of the measurements with 1 at% [49]. One paper quantifies only the metal impurities in the film without standardization and specifies the accuracy with 0.01 at% [114]. In [40], at least the type of instrument, a Jeol IXA-3A, is specified, but further only the use of noncertified calibration standards is stated.

EPMA has obviously been applied for the quantitative analysis of silicon oxynitride films, but the method used for the calibration of the instrument, the standards used, and the figures of merit like repeatability, reproducibility, and accuracy, together with the optimized analysis parameters are not described. This leads to the conclusion that the authors of these papers did not scrutinize the applicability of this analytical method for oxynitride films and, therefore, did not spend much effort in optimizing and evaluating their method of EPMA analysis.

The EPMA instrument used in [115] was an ARL-EMX-SM electron microprobe, and the investigated films had a thickness of 200–300 nm. In order to confine the electron-excited volume of the film, accelerating voltages of 4 and 5 kV were applied. Al_2O_3 and Si_3N_4 were used as standards, and the in-

tensities were corrected for absorption and scattering, yielding a relative accuracy of generally ±5 %. The precision is given as 2–3 % at the 95 % confidence level. The lines observed were Al Kα, O Kα, and N Kα.

Also in [116], EPMA was applied for the quantification of SiO_XN_Y films. The instrument in this case was a Cambridge scanning electron microscope with a Kevex microprobe, and EDX was used. Some limitations for this method of analysis are given, such as the necessity to apply calibration standards, the lower accuracy in the determination of light elements, and the closeness of the oxygen and nitrogen peaks as a source of error in the deconvolution. The authors make the wrong statement that bulk standards, though available for SiO_2, cannot be used, because they give wrong results if used for the quantification of films. As a complementary method, the technique of RBS was used. The deviation in the results with a higher nitrogen content observed by EPMA than by RBS was attributed to the poor suppression of the background during the nitrogen peak deconvolution. Finally, with the interpretation of IR spectra, they conclude a mixture of SiO_2 and Si_3N_4, since a peak expected for N–Si–O at 1100 cm^{-1} did not occur.

SiAlON samples prepared by carbonitridation of clays were investigated in [117]. The powders obtained were pressed and analyzed by XRD and IR. Si_2N_2O, AlO_XN_Y, and Al_2O_3 are observed besides the principle β-SiAlON phase, but no diffractograms are given. Only the ratio of Si/Al is given, which was determined by EPMA.

Due to recent developments in EDS detector sensitivity and resolution, improved computer power and software, this common method of analysis has been chosen as the main method of analysis for the oxynitride films by our working group and much care was invested in the proper setup of the instrument, standardization, evaluation, and statistical interpretation of all films that were produced by the deposition process. The EPMA instrument used for [34,81,118,119] was an ARL SEMQ equipped with the Voyager II X-ray Quantitative Microanalysis 2100/2110 EDX system from Noran instruments. The detector used was a SiLi detector with a Norvar window, which allows analysis of light elements down to boron. The take-off angle of the detector is 52.5°. The instrument was operated by the Voyager software, which includes peak deconvolution with multiple least-squares fitting and matrix correction by the PROZA program utilizing the $\varphi(\rho z)$ model. All measurements were performed at a beam-accelerating voltage of 5 kV. In this case, the information depth calculated by the PROZA curves is about 350 nm. The measurements of the samples were performed with a beam current of 60 nA and a sample current of 10 nA. An area of 40×40 μm^2 was scanned with high frequency for each measurement.

It is shown in [118,119], that EDS-EPMA is a fast and reliable analytical method for the quantitative analysis of homogeneous oxynitride films, if an appropriate standardization procedure is applied. The main feature is the calibration of the instrument, which can be used for all compositions, independent of the surface morphology of the samples, and without recalibration unless the accelerating voltage is changed. This is proven by the fact that the measurements of oxynitride films used in the publications were performed parallel to the sample deposition over several months. During this period, the calibration was checked, but it was not necessary to recalibrate the instrument. By application of thin film analysis software, films down to 20-nm thickness can be quantitatively analyzed, which was demonstrated in [119]. Since the aim of the work was not trace analysis, but the development of an analytical method for the quantification of the main components in oxynitride films, optimized EDS-EPMA turned out to be the fastest and most accurate method available.

In addition to the quantitative bulk results given in the publications, EPMA can be utilized for lateral distribution analysis. The surface of some of the films investigated, depending on the sputtering parameters during deposition, showed droplets resulting from arcing at the target surface. By elemental mapping, small droplets on SiO_XN_Y films were investigated, but no difference in elemental composition to the film material itself could be detected. For a very large droplet, elemental distribution maps for silicon, oxygen, and nitrogen exhibited an excess of silicon. Thus, if an arc at the target surface emits a particle of sufficient size during sputtering, this particle melts at the surface where it also partly reacts with the reactive gases in the plasma, but the core of the particle remains unreacted target material.

Further measurements with a WDS instrument were performed on SiO_XN_Y films with a Jeol JXA-88900 WD/ED Combined Microanalyzer. The key feature of this system is a fast-scanning WDS detection system with very high sensitivity. Thus, it is possible to reduce the counting time and the sample current to low levels, while keeping the detection limits below 1 at%. This detection system allows one to scan the background and the peak area of an analytical peak during each analysis. With this technique, peak shifts and peak distortions can be detected and eliminated by integrating the peak area between appropriate background correction positions, which can be selected for each sample in a reprocessing step. Each element was measured simultaneously but with different optimized crystals. Measurement conditions were 5 keV accelerating voltage, 3 nA beam current, 2 s counting time, and an analyzed area of 100×100 µm^2.

The Jeol EPMA with a new fast-scanning WDS detection system was also tested for the possibility to quantitatively analyze SiO_XN_Y and AlO_XN_Y films. Spectra of the nitrogen and oxygen signal for the SiO_2 and Si_3N_4 standards as well as two SiO_XN_Y samples were measured and show similar chemical bonding and surface structure since no peak broadening or peak shift is observed. The new developments in the detection system together with the stable peaks of the oxynitride films allowed easy quantification of six representative oxynitride films by WDS and the results were compared to the EDS results (Table 2).

Table 2 Comparison of the quantitative results obtained by WDS and EDS EPMA.

Atom fraction Si/%		Atom fraction O/%		Atom fraction N/%	
WDS	EDS	WDS	EDS	WDS	EDS
43.2	43.6	1.4	0.5	55.4	56.0
41.3	41.5	10.4	10.9	48.2	47.5
36.8	37.2	36.7	34.4	26.5	28.4
35.1	33.9	52.1	53.6	12.9	12.6
35.4	34.0	56.2	57.9	8.4	8.1
32.7	31.3	67.3	68.3	<0.2	0.3

However, the disadvantage of WDS again became obvious when a quantitative line scan was tried on one sample. The quantitative results for this point analysis, gained with the calibration on a 100×100 µm^2 area, deviated up to 20 % from the known composition. Therefore, it was necessary to completely recalibrate the instrument for spot analysis. This of course is a very time-consuming drawback, since the calibration cannot be used over a period of several months like for EDS, but has to be redone for each change of the detected area, as well as after changing the sample.

Thus, for EPMA, the calibration of the instrument is the most important factor for appropriate analysis as well as an instrumental design that favors quantification of light elements. Since no standards are available for oxynitride films, quartz and alumina standards can be utilized, but special care has to be taken in the preparation of the nitride standards, since to our knowledge no certified stoichiometric standard films applicable for EPMA analysis are commercially available.

5.2 Auger electron spectrometry

AES is one of the most frequently applied methods for the analysis of thin films and surfaces due to its high surface sensitivity and small analyzed area. Therefore, more publications on the analysis of oxynitride films by AES can be found than for EPMA. Silicon, oxygen, and nitrogen have a low atomic number and thus a high Auger yield. The silicon peaks are sensitive to the chemical environment, which permits distinguishing among the silicon compounds. In most publications, the authors do not mention how they dealt with the charging sample.

One problem that occurs in AES analysis of oxynitride films is the decomposition of the film due to the high-energy electron bombardment. In [120], argon sputtering and AES analysis of the films were performed alternately, using 500 eV argon ions with an angle of incidence of 34°, and an electron beam energy of 5.0 keV with a current density $<10^{-3}$ A/cm^2. The total dose during one AES spectrum was kept below 1 C/cm^2, which is described as sufficient for avoiding electron-induced decomposition. The high-energy silicon peak (KLL) was used for quantification due to the lower sensitivity of its peak shape to the chemical environment. The nitrogen and oxygen (KLL) peaks were also measured in the N(E) mode. The detection level of oxygen is given as 0.1 at%. Decomposition of the silicon nitride surface by the ion beam could not be avoided but kept at a constant level. The accuracy of the Si(KLL) measurement is specified as 2 %, with decidedly worse accuracy of the oxygen and nitrogen measurements resulting in an average value of 10 % for the peak area ratios O/Si, N/Si, and O/N. Stoichiometric SiO_2, Si_3N_4, and SiO_XN_Y (x/y = 0.36) films were used as calibration standards. he thickness and the stoichiometry of these standards were determined by RBS. The same lines in the N(E) mode were used in [121] with a primary electron beam energy of 5 keV and a beam current of 2×10^{-7} A measured at an incident angle of 80° in order to prevent charge build-up. The Si(KLL) transition was used because of its relative insensitivity to the chemical environment. The relative sensitivity factors for N and O, obtained from measurements of not described Si_3N_4 and SiO_2 films, were applied without adapting to the SiO_XN_Y films assuming the same 10 % uncertainty obtained in [120]. In [22], the O/N ratio of films deposited on silicon obtained by AES and RBS were compared and a good agreement was achieved for 10 oxynitride films with thicknesses <60 nm. RBS spectra were recorded under normal incidence and channelling conditions (incidence angle = 54.71° to sample normal, detector counts particles scattered at 5° from surface), and concentration vs. depth profiles of oxygen and nitrogen were calculated assuming the same atomic density for oxygen and nitrogen as in SiO_2 respectively Si_3N_4. The channelling conditions resulted in a much lower background originating from to the silicon substrate and in an increased depth resolution due to the longer travelling distance in the film. Ellipsometry measurements delivered an overestimated thickness in reference to RBS, because a thin oxide layer at the interface between film and substrate was not included in the ellipsometry evaluation. The inspection of the Si(KLL) signals in the AES spectra also led the authors to the conclusion, that in silicon oxynitride films the silicon atoms are randomly surrounded by oxygen and nitrogen atoms.

Also in [122], the results obtained by AES were compared to RBS results. The AES measurements were performed on films deposited on metallized quartz slides with a Varian 120 CMA spectrometer in the derivative mode. The difficulties in the application of AES are described as uncertainties by the application of atomic sensitivity factors in the analysis of compound materials, the transport of the samples in the air, and the sputter-cleaning of the surface, necessary because of the thin oxide like surface layer, which introduces preferential sputtering effects. The authors concluded that the determination of the silicon content was almost impossible with AES under the chosen conditions after argon ion sputtering, since the peak shape of the Si LVV changed significantly. The usefulness of the sputter cleaning process was questioned even more after the observation that, at the residual gas pressure of the instrument of $1 - 3 \times 10^{-8}$ Pa, an increase of the oxygen content supposedly from the residual gas was evident. The authors concluded that the verification of the AES results by an independent technique was necessary. They chose RBS because it would give an absolute measure of the bulk composition. The comparison led to the conclusion that the ratios of O/(O+N) evaluated by AES are 10 % higher than those taken from RBS. The authors conclude AES to be useful for the quantification of compound materials if high precision is not requested and advise the use of calibration experiments.

AES and RBS were also utilized in [25]. The AES depth profiles were taken by a Jeol instrument in the derivative mode. Films with known composition without further specification were used for the calibration of the instrument for the quantitative analysis of silicon, oxygen, and nitrogen. For RBS, a He^{2+} beam with an energy of 2 MeV was used, and the quantification of the depth distribution was performed without standards through spectral peak heights and elemental scattering cross-sections. The

content of hydrogen was determined by ERDA with ^{35}Cl at 30 MeV. RBS and AES results showed good agreement.

AES depth profiling was applied in [21], but only the Auger yield vs. the sputter time is given in the depth profiles, not the concentration of silicon, oxygen, and nitrogen. The O/N ratios in the films were derived from the spectra using AES sensitivity factors and were compared to the RBS results of the films. In this publication, no systematic deviation of the AES results from the RBS results was observed, but no details are given on the instrumental parameters and on the sputtering parameters. Together with the film thickness obtained by RBS and the sputter profiles of AES, the dependence of the sputter rate on the O/N ratio of the films was established for a 2 keV Ar^+ ion bombardment.

A Perkin–Elmer Model 10-155 was used in [123] to analyze films with a thickness in the range of 1–3 nm. Si, SiO_2, and Si_3N_4 were used as standards. Argon sputter depth profiling was applied in some cases. The results were compared to SIMS and XPS and a mechanism for the nitrogen incorporation in ultrathin oxynitride films grown by low-temperature remote plasma-assisted oxidation was derived.

Another publication [124] deals with the interpretation of the $Si(L_{2,3}VV)$ and O and N(KVV) Auger lines in the first derivative mode. The samples were sputter-cleaned in order to remove the oxidized surface layer, which forms rapidly at exposure to air. AES data taken during argon ion sputtering were slightly distorted due to the Ar present in the system. The observation of this group was that SiO_2 films were much more changed by the 2 keV, 1 μA electron beam than pure Si_3N_4 films. The feature at the high-energy side of the Si peak was correlated to the oxygen content of the films, negating the former assumption of elemental silicon as the source of this feature. The peak shift of the oxygen signal to higher energies relatively to the SiO_2 signal was assigned to a weaker bonding of the oxygen in oxynitride films than in SiO_2. The conclusion was that the silicon oxynitride films were amorphous polymers of Si, O, and N. A tetrahedrally bonded SiO_2 structure was found only at oxygen concentrations >50–60 at%. No further information is given on the calibration of the instrument and standards, the lowest oxygen concentration is specified as <0.5 at% without standard deviation or detection limits for silicon and nitrogen. The refractive index vs. at% oxygen for 6 films is given, and it changes from 1.97 at 0 at% oxygen to 1.45 at 64 at% oxygen, but the wavelength is not specified. In [73], the derivative mode was used to determine the fractions of silicon, oxygen, and nitrogen in SiO_XN_Y films, too. In this publication, a primary electron beam with 3 μA beam current and an energy of 5 keV was used together with an argon ion beam for the sputtering of a 3×3 mm^2 area with parameters chosen in order to achieve a sputter rate of 0.04 nm/s while minimizing knock-on effects. The peak-to-peak heights of the Si, O, and N(KLL) peaks were used to determine depth profiles vs. sputtering time. The films had a thickness of ~40 nm.

The oxygen-to-nitrogen ratio was determined by AES in [64] with a 2 keV, 0.5–1.0 μA electron beam and on sputter-cleaned samples using a 1–4 keV Ar beam. The damage of the ion beam increased with higher kinetic energy, and the electron beam damage increased with higher integrated electron dosage in SiO_2 films. In contrast to these results, silicon nitride films were damaged in a stronger way by low-energy Ar ions (1 keV) than high-energy ions (4 keV), while the electron beam effect was similar to the results found for the oxide films. The composition of oxynitride films was determined by AES in combination with IR. The results for the damage tests of ion and energy beams were according to those found for the nitride and oxide films. In the spot mode, the damage of the electron beam was higher than in the raster mode. The ion beam was supposed to produce Si–Si bonds by preferential sputtering of nitrogen and also oxygen. In [10], the authors come to the same conclusions, including the fact that relative concentrations of Si, O, and N from the derivative spectra cannot be obtained due to the changes in the Si(LVV) line shape with changes in the oxynitride composition. In this case, all data were taken with the Ar ion beam on.

Ion and electron beam effects on the Si(LVV) line were also investigated in [125] in a UHV chamber equipped with a single-pass cylindrical mirror analyzer. The Ar ion bombardment (0.5 3 keV, 40°

to sample surface) in this study also led to preferential sputtering of oxygen and nitrogen and the formation of Si–Si bonds corresponding to an elemental silicon peak. The effect was stronger for SiO_2 than for Si_3N_4, and almost negligible for an oxynitride film with O/N = 0.37. Also, the electron irradiation (0.1–3 keV, normal incidence, 20–200 μm diameter) was described as producing electron-stimulated desorption of oxygen and nitrogen. Silicon oxynitride films with an atomic ratio of O/N = 0.2–1 did not show any influence of the electron beam irradiation. While the AES spectra were recorded in the first derivative mode, low-energy EELS spectra, also investigating changes introduced by the argon ion sputtering, were measured in the second derivative mode using a sine wave modulation technique of the CMA. In [126], the authors concluded from the AES spectra that oxygen and nitrogen were mixed on an atomic scale in the oxynitride films, not forming a mixture of SiO_4 and Si_3N_4 tetrahedra. This work was also mentioned in [97], where the authors indicate the problems of the investigations, such as specimen charging, electron beam-induced damage and sample decomposition, the inherent high, sloping, inelastic background, etc. The authors of this publication thus prefer XPS.

In [24], a ternary composition diagram of silicon oxynitride was given and the atomic structure was described as fourfold-coordinated Si atoms bonded to either O or N atoms. N atoms were threefold-coordinated and bonded only to Si atoms, all O atoms were twofold-coordinated and also bound only to Si atoms, no Si–Si and N–O bonds were present. The changes in the Si(LVV), O(KLL), and N(KLL) lines were recorded on line on films with a thickness of approximately 130 nm.

Depth profiles of 10–100 nm thick SiO_XN_Y films are shown in [65] as peak-to-peak heights vs. sputtering time. The films were sputtered with 1 keV Ar ions, but no details about the analysis parameters are given. The detection limit of AES was given as 1 at%. Increased oxygen concentrations were observed at the surface and at the interfaces between film and silicon wafer substrate. With 6 films, a linear correlation between the oxygen and nitrogen concentrations and the refractive index was suggested for LPCVD films, while for PECVD films the variation was described as nonlinear. The reason for this behavior was sought in the large amounts of hydrogen in these films. The refractive index of PECVD oxynitride films was found to vary between 1.47 (SiO_2 with 3 at% N) and 1.95 (Si_3N_4) at 632.8 nm, the refractive index of LPCVD films between 1.46 and 2.0. The authors do not give details on the quantification procedure. Detailed spectra of the Si LVV peak in SiO_2, Si_3N_4, and SiO_XN_Y are given. The main signal shifted from 88.5 eV for Si_3N_4 to 76 eV for SiO_2, the peak broadened for the SiO_XN_Y film, but only one continuous Si(LVV) peak was observed, supporting the RBM. The XPS analysis of these films also confirmed the surface oxidation of the films. The binding energy shift due to sample charging had to be corrected by assigning to the surface carbon signal.

In [15], the sensitivity factors were determined by measurement of two samples with RBS, which was described as an absolute measurement technique. The Si sensitivity factor was assumed to be 1. The AES measurements were performed with a 2 keV electron beam with 200 μA at normal incidence. Si(LVV), O(KLL), and N(KLL) peaks were studied. The other multilayer films were also investigated by IR for radiative cooling, and quantitative AES depth profiles were obtained by alternating ion sputtering with analysis.

Other publications did not bother with the quantification of the AES depth profiles or line scans at all, but simply used the intensity profiles [6,127–131] in order to check the homogeneity of the films or the effect of electron beams on the surface. An SEM image of the impact area of the electron beam is given in [127]. Such qualitative depth profiles of Rugate filters with 10 sinusoidal periods and a linearly graded SiO_XN_Y film are also given in [132]. The rather diffuse interfaces obtained are attributed by the authors to atomic mixing and knock-on effects associated with argon ion sputtering.

Micro-AES was performed with a JEOL Jamps 10 S instrument and the Si(LMM), O(KLL), and N(KLL) signals were investigated in [133]. No details on the instrumental parameters are given.

AES measurements of AlO_XN_Y films deposited on a silicon wafer (100) by reactive rf sputtering were performed in [134] with a PHI-500 instrument. The thickness of the films was determined by profilometry with a precision of 0.5 nm and an accuracy of <1 nm, the refractive index by ellipsometry at 633 nm. The film thickness was found to be approximately 75 nm, the composition of one film ana-

lyzed by AES depth profiling was determined as 41.4 at% aluminum, 31.4 at% oxygen, and 25.7 at% nitrogen, without comments on the quantification procedure. Additionally, 1.5 at% silicon were found, probably resulting from the silicon substrate. The authors state that similar to the formation SiO_XN_Y also aluminum reacts stronger with oxygen than nitrogen. Hence, the oxygen content of the reactive gas mixture had to be controlled very carefully. The correlation between the refractive index and the oxygen concentration was found to follow a concave curvature between the Al_2O_3 and AlN end-points. The authors simply describe their films as a polyfilm combining the good properties of Al_2O_3 and AlN.

Quantitative AES depth profiling of AlO_XN_Y films on GaAs substrates with thicknesses <110 nm was also employed in [29] in a Physical Electronics 548 ESCA/AES system with a 3 keV, 10 µA electron beam and a 2 keV sputter beam for depth profiling. AlO_XN_Y films were produced unintentionally because of a leak in the argon gas line, but even when this problem was eliminated, the oxygen level still was about 5 at%. Free aluminum (68 eV), Al_2O_3 (52 eV), and AlN (57 eV) were distinguished by the energy of the Al AES line in the direct mode. The approximate bulk composition was then determined by the measured peak heights and sensitivity factors. The ratio of Al_2O_3 and AlN was also qualitatively determined as a function of the relative peak heights of the lines at 52 and 57 eV. The depth profiles of the films show a small increase in oxygen at the surface due to oxidation by air and at the interface between film and substrate, with oxygen mostly bonded to aluminum. The films were annealed at 400–1000 °C under hydrogen atmosphere and the depth profiles after this treatment showed further oxidation and a more pronounced pile up at the interface, suggesting transport of oxygen through the film, and diffusion of As and other components. The films deposited on Corning 7059 microscope glass in general showed an average transmission established by spectrophotometry close to 90 % over a spectral range of 200–3000 nm. The sample surface before and after annealing and with/without prior sputter etching of the substrate was recorded by optical microscope photographs with a magnification of 400. The electrical properties as encapsulating films were investigated.

AES analysis in combination with argon ion milling in a PHI 590 spectrometer at an electron beam voltage of 3 kV and a current of 4 mA/cm^2 was applied in [135]. The sputtering was performed with an argon ion beam with 2 keV at an incidence angle of 50°, the beam was rastered over an area of 2.8 mm^2 in order to obtain a smooth crater bottom. The quantitative depth profiles of the ~10 nm thick films are shown.

AES measurements were performed by us using a Leybold LHS 12 electron spectrometer with sputter depth profiling. In order to avoid charging of the samples, the secondary electron yield had to be kept at values greater than one, which was achieved by selection of the appropriate primary electron energy and tilt angle of the sample. Furthermore, a suitable ratio between the argon ion current for the sputtering process and the electron current for the Auger electron excitation had to be chosen. The best instrumental set-up was a primary electron energy of 1.3 keV at an incidence angle of 60° with respect to the sample normal and an electron current of 5 µA. The AES investigations were performed alternating with sputtering of the sample by a scanned 4 keV Ar ion beam. The measured lines were Si(LMM), O(KLL), and N(KLL) [34].

A strong distortion of the peak shapes of the Auger lines in the derivative mode was encountered. Although the quantitative analytical data were derived from the peak integrals, a nonlinear correlation between composition and Auger intensity was observed in [34], similar to [97]. The spectra show the decomposition of the oxygen-rich AlO_XN_Y film. The feature of metallic aluminum at the theoretical value of 68 eV becomes stronger with prolonged ion and electron bombardment, while the feature typical for aluminum in Al_2O_3 at 51 eV diminishes. The conclusion has to be that quantification with AES is not possible if only oxide and nitride standards are available. AES depth profiling can be used for quantitative analysis of oxynitride films only if a matrix-matched oxynitride standard with a similar composition to the sample is available. Even this is possible only for homogeneous films after steady-state conditions are reached.

Once again, it has to be emphasized that the most important difficulties are the correct standardization of the method and the unavailability of certified standard material.

5.3 Electron microscopy

Scanning electron microscopy is used for the determination of the film thickness [136], the morphology [137], and the investigation of the sample surfaces and fracture edges [75,138]. The structure of the films is often determined by TEM through micro-diffraction.

Scanning electron microscopy is often used together with profilometry measurements to determine the film thickness and the uniformity of the thickness, such as in [139], where a Dektak 3030 profilometer, Veco Instruments, was used together with electron micrographs of fracture edges on a silicon (100) substrate. The uniformity of the film thickness was ±8 %. The films need to adhere very well in order to make such measurements on fracture edges possible.

Scanning electron micrographs of film surfaces and rupture edges were used in [23] together with XRD and TEM (selected area electron diffraction) to assign the sputtered films as amorphous without structure or voids, and samples were also included which showed columnar growth and porosity in SEM. The limit of resolution of SEM micrographs of surfaces and rupture edges is given as 10 nm in [39]. Also, changes of the surface structure after exposure to condensed water [49] or other surface treatments were investigated by SEM. TEM and SEM are used as well for the investigation of crystallization processes [140]. Silicon oxynitrides needed a higher temperature for crystallization and longer vacuum annealing times than silicon nitride, but shorter than silicon dioxide.

The SEM micrographs of the surface of targets used for laser ablation are shown in [55] and melting-solidification phenomena become obvious, while micrographs of the resulting films show small grains resulting from ejected droplets.

Extensive investigations on AlO_XN_Y films were performed as early as 1975 [141]. The film thickness and the refractive index (1.72 to 2.05) were determined by ellipsometry at 546.1 nm and the composition by EPMA. Transmission electron microscopy was applied on films deposited on silicon, which was chemically etched away. The exposed films had a thickness of ~50 nm and were transparent to the 100 keV electrons, but the charging effects allowed micrographs to be taken only in closest proximity to the remaining silicon. Diffraction patterns were also determined. In the diffraction patterns of the films, three different polycrystalline phases were observed. One crystalline film was determined as AlN (0 at% oxygen). With increasing oxygen content, oxygen-substituted nitrogen in the films and the AlN diffraction patterns became more diffuse as the crystal grains became unresolvable. Dark field electron microscopy of films showing diffuse halos did not reveal evidence for a polycrystalline material, and, therefore, these films were assumed to be amorphous. Other diffraction patterns were described as AlO_XN_Y spinel (57 at% oxygen), Al_2O_3 (60 at% oxygen), AlN phase (8 at% oxygen), and zeta-alumina (13 at% oxygen). The oxynitride films were described as a pseudo-binary system. In the publication that deals with the deposition of the films [115], it is stated that "solutions" of Al_2O_3 and AlN should yield noncrystalline films because of the increased configuration entropy.

The thickness of aluminum oxynitride films on glass substrates was determined by a field emission SEM with 2–7 keV on cross-sectional fracture surfaces. The magnification of the Hitachi S4100 instrument was calibrated by the use of polystyrene spheres in [142]. The films were deposited with about 50 cycles of 100 nm and show columnar growth, but also particles with the same growth features as the films. According to the authors, these are the results from irregularities of the substrate. The composition of the films was determined as variations of the XPS signal intensity with depth.

HR-TEM micrographs with a resolution of 0.21 nm revealed polycrystalline PVD-deposited AlO_XN_Y films and the selected area diffraction patterns are given in [143]. The grain size varied between 5 and 30 nm.

In the investigation performed by our working group, only the imaging mode of the scanning electron microscope was exploited. The contrast consequently was a mixture of topographical and elemental contrast. The instrument used was a Jeol 6400. The accelerating voltage was set to 15 keV and the magnification was in the range of 50 000–60 000. The optimum resolution of the instrument at 30 keV is 3.5 nm. The standards that were applied for the calibration of the film thickness determination are

distributed by Agar Scientific, England. The instrument was calibrated with a Sira Test Specimen S170 with a fine grating of 2160 lines/mm (calibrated specimen no. A204) with a spacing between the rulings of 0.463 μm. Since the oxynitride films deposited on silicon substrates did not show sufficient conductivity, all samples had to be coated with a thin gold or carbon film. The samples were fractured and mostly the fracture surface was studied in the electron microscope.

The pictures of the fractures revealed well-adhering, homogeneous films, without recognizable microstructure. The film thickness was determined at three different locations of the fracture for each sample and the mean value was calculated. All of the film thickness values given in this work are based on these SEM measurements, on profilometry measurements, and on ellipsometry measurements. The accuracy of the thickness measurement by SEM was determined to be ±10 nm. The surface of the films deposited by reactive dc-magnetron sputtering was generally smooth with the exception of small droplets occurring now and then, stemming from arcs at the target during sputter deposition of the films. For extremely inferior deposition parameters, the film surface was covered with small droplets of different shapes and also small holes could be observed.

A general difficulty in the examination of thin nonconducting films is the necessity to coat the samples for improved conductivity, which further deteriorates the contrast between the substrate and the film in the cross-sectional view, which turned out to be low in the case of SiO_XN_Y and AlO_XN_Y on silicon substrates. The fracturing often causes the film to chip off at several places and edge effects can be misinterpreted as very thin films. Nonetheless, this method is considered to be a standard method in order to evaluate the surface quality, adhesion, and thickness of the films.

5.4 Electron energy loss spectrometry

This analytical method is used rather rarely for the analysis of silicon oxynitride films. Nevertheless, interesting results were obtained by some authors.

Reference [144] especially deals with the consideration if silicon oxynitride films are a solid alloy of SiO_2 and Si_3N_4 with covalent bonds linking together SiO_2 and Si_3N_4 molecules. This material should exhibit properties following what the authors call a two-mode behavior, identical to the RMM. Most publications observe a one-mode behavior and therefore assume a mixture of Si–N and Si–O bonds on an atomic level, which is confirmed by this paper. The IR optical response of such an alloy can be modeled by the Bruggemann effective-medium theory. HREELS measurements were performed in order to gain infrared data of SiO_XN_Y films. The stoichiometry of the films was determined by AES, which was calibrated by RBS. The HREELS measurements were performed in a UHV chamber with an electron beam energy of 7 eV. A second defocused electron gun with 2 keV was used for the neutralization of the charging effects. Surface phonons (long-wavelength optical vibrations) had to be considered as modes of propagation of molecular vibrations in the amorphous SiO_XN_Y films. The author described the effect as a broadening of the optically active lines and an increase in the number of IR-active vibrations. A broad background, which could not be explained by the authors, was observed in the measurements and included in the calculations. The best achievable energy resolution was 90 cm^{-1} in these amorphous dielectric films. The observed loss peaks for an oxynitride film with a composition given as N/(N+O) = 0.37 at 1190 cm^{-1} and another film with N/(N+O) = 0.80 at 1070 cm^{-1} were defined as multiple component structures. The peak at 480 cm^{-1}, which occurred in both spectra, was defined as the Si–O rocking vibration. A deconvolution process for the peak at 1190 cm^{-1} led to a small contribution around 910 cm^{-1}, assigned to a mixing of Si–O and Si–N bending vibrations, another small shoulder at 1420 cm^{-1} was attributed to a small hydrocarbon contamination, and the mode at 1600 cm^{-1} was defined as a combination of intense first-order peaks. The deconvolution for the peak at 1070 cm^{-1} yielded 890 cm^{-1} for the mixing of Si–O and Si–N bending vibrations and a decrease in the intensity of the 1420 and in this case 1650 cm^{-1} feature. Furthermore, the amorphous character of the oxynitride films was confirmed by analyzing the films at different angles. In this publication, an exponential dependence of the main absorption peak wavelength on the N/(N+O) ratio was observed. The same group of authors

investigated films with the same analytical parameters in an earlier publication [145], in which the instrument is given as a Sedra Isa-Riber and the argon ion sputtering was performed with 1 keV energy. In that publication, a film with a composition stated as $SiO_{1.3}N_{0.6}$ was investigated.

REELS and LEED analyses were performed in [146] together with AES on ultrathin oxynitride films with a thickness <2 nm. The instrument used was a single-pass cylindrical mirror analyzer with an energy resolution of 1.1 eV at a primary ion energy of 80 eV and 4.0 eV at 1000 eV. With the REELS measurements, the gap widths of the resulting films were investigated.

The theory of EELS measurements of thin oxynitride films on NiAl surfaces is described in [147]. The samples were also investigated by LEED and AES to detect the growth and crystallinity of the aluminum oxynitride films. The same group of authors used HREELS, AES, LEED, and EELS to analyze the growth of the same films in [148].

6. ION BEAM ANALYTICAL TECHNIQUES

Ion beam techniques are generally more expensive than electron beam techniques. Nonetheless, this type of analytical technique is used quite frequently when a so-called absolute or standardless method is necessary.

6.1 Rutherford backscattering spectrometry

The oxidation behavior of silicon oxynitride films with a thickness of 40–150 nm was investigated in [149] with RBS and ERDA. The authors first mention that both methods are quantitative and thus measured the absolute amount of nitrogen and oxygen atoms per cm^2 without calibration. All spectra were recorded under channelling conditions, which were used to reduce the background of the silicon substrate and therefore increase the accuracy of the N and O peak area detection. The oxidation of the silicon nitride films was found to proceed from the surface in a layer-by-layer mechanism. The influences of the water content in the oxygen atmosphere, the temperature, and the effect of hydrogen on the oxide growth were examined. The influence of the film thickness on the quantitative results for the oxygen content in the films had to be eliminated in order to make the results comparable. This was achieved by the prediction that in all cases the silicon peak area was solely influenced by the film thickness. For films with oxygen contents lower than 2×10^{16} cm^{-2}, ERDA was applied, because the sensitivity of RBS limited the accuracy of the determination of the differences in the oxygen content.

RBS is often applied for the verification of other analytical techniques or as a calibration method such as in [122], where the results of RBS were compared to the results of AES. He^+ ions with an energy of 0.8 MeV were used and resulted in overlapping nitrogen and oxygen peaks, which had to be deconvoluted. The advantage of RBS over AES in this publication was the insensitivity to thin surface contamination films. The accuracy of a single measurement was given as ±5%. The results for the O/(O+N) ratios of AES turned out to be 10 % higher than the RBS results for the investigated films. The conclusion was that the methods showed a relatively good agreement, if high precision was not requested. In [144], RBS was used to calibrate the AES instrument. The same group of authors also investigated the hydrogenation of AlO_XN_Y films with RBS measurements [150]. The substrate material for these measurements was beryllium, and 0.8 MeV He ions were applied. Together with this method, IR transmission measurements on silicon substrates, optical transmittance and reflectance spectrophotometry, refractive index determination by Brewster angle determination following the Abelès method, and interferometric thickness determinations with an accuracy of ~5 %, were used. The values of the refractive index scattered due to the measurement accuracy itself and due to the errors in the AES and RBS measurements of the O/(O+N) ratio due to the difference in depth sensitivity and also oxygen adsorption of the films.

RBS is applied in [21] for the determination of the film thickness. For this purpose, the authors made the wrong assumption that the oxynitride film thickness is similar to that of a silicon dioxide plus a silicon nitride film with the same overall composition. Since RBS determines only the film area density in atoms/cm^2, the film volume density in atoms/cm^3 has to be known in order to calculate the thickness from the ratio film area density divided by film volume density. The authors of [21] did not take this into consideration, and used only the bulk densities of SiO_2 and Si_3N_4. The difference in the density of deposited films and bulk materials was not taken into account. The film thickness was also determined by ellipsometry and the results show a systematic deviation. The film thicknesses obtained by RBS always were lower than the thickness obtained by ellipsometry. The authors finally had to admit that SiO_XN_Y films might have a lower density than the bulk material Si_3N_4 and SiO_2. Also in this publication, the composition was given by the ratio O/(O+N), the silicon content was not given as a result of the RBS measurements. The results were corrected for the contribution of the native oxide layer on the silicon substrates. Depth profiles of the films were performed by AES. Together with the oxygen to nitrogen ratios obtained by RBS, this method was also utilized under channelling conditions in [21] to calculate the effective amount of excess silicon in the oxynitride films. It was found that no such silicon atoms were present and a small excess of oxygen or nitrogen (1–4 at%) was calculated.

An interesting combination of measurements was applied in [68], where the composition of several films was analyzed by RBS, and optical and electrical data were investigated. The films were backed by a Be foil. Alpha particles at an energy of 2.4 MeV were used to avoid nuclear reactions. The backscattering yield was analyzed with an energy dispersive detector at 12° off-normal. The authors emphasize that working with thin films facilitates the RBS spectra, since no overlapping peaks are encountered and with Be as a substrate material even carbon can be analyzed. The film thickness in this publication was not derived from the RBS spectra but from stylus and interference measurements. Quantification was achieved considering the energy losses, the capture cross-sections of the atomic species, and the background. Thus, in this publication, the composition of the films was given as SiO_XN_Y with specified x and y values.

RBS with 2.28 MeV He ions at scattering angles of 10–160° from the incident beam was performed in [151] together with HFS and SIMS measurements. Channelling of the ions into the single-crystal silicon substrate was exploited to analyze the O and N content of the film. This way, the authors state that the silicon background was reduced by 95–97 %. The accuracy of the combination of RBS and HFS results is given as ±7–10 % absolute with a repeatability of ±5 %.

In [11], random and channelled RBS was applied. The uncertainties in the stopping power data used to extract the atomic composition resulted in an uncertainty of ±10 %.

In many other publications, RBS is only mentioned as the technique used for the determination of the film composition [60,136], while the main object of the paper lies in another area.

RBS with 1.892 MeV He^+ was applied with an accuracy of better than 1 % for the analysis of AlO_XN_Y films deposited on graphite substrates [46], which is inconsistent with the other data given in this publication. When the standard deviations of the thickness and composition values, which were in the range of ±10–50 %, are considered, it becomes obvious that the accuracy of 1 % claimed for RBS is just a theoretical value which can be achieved under optimum circumstances, but is not attainable in this case. Graphite was used, because the silicon and oxygen signals of a glass substrate would have overlapped with those of aluminum, oxygen, and nitrogen of the films. The films were less than 100 nm thick in order to prevent an overlap of the oxygen and nitrogen backscattering peak. The stoichiometry was given in the form of x and y values for the formula AlO_XN_Y. The values for x varied between 0.02 ± 0.01 and 0.52 ± 0.04, the y value varied between 0.55 ± 0.01 and 1.58 ± 0.10. The films also showed very high packing densities, so that water could not migrate through the films, but they showed an oxidized surfaced layer of 15 ± 7.5 nm thickness. The x and y values included this oxidized surface layer. In [47], the detection limit of RBS for nitrogen was specified with ~0.4 at%.

RBS at a glancing incidence of 168° with 2 MeV He ions was used in [152]. The films were also analyzed by ellipsometry and FTIR. A linear correlation between the infrared wavenumber and the re-

fractive index was observed. The EMA model was used for the calculation of the refractive index with SiO_2 and Si_3N_4 as reference spectra and the assumption of an abrupt interface. The refractive index varied between 1.5 and 1.95. The calculated values for the oxygen content in the films were significantly lower for the EMA model than for the RBS results. The deviation is in the range of 10 to 50 %. The authors state that the reasons for under-stoichiometric films are disproved by RBS and also no higher film density was observed. Thus, the authors state that the one-layer model must be wrong or no microscopic mixture was obtained. The authors estimated the standard deviation of the RBS with a maximum of 25 %.

SiAlON films were produced by sputtering in [153] and analyzed by RBS. Implanted SiO_XN_Y and AlO_XN_Y films were also analyzed by RBS with 2 MeV He ions detected at 140°. For depth profiling of complex layers, NRA was used in combination and the reactions $^{15}N(p,\alpha\gamma)^{12}C$ at 429 keV and $^{18}O(p,\gamma)^{19}F$ at 1928 keV were used. The deconvoluted depth profiles of the NRA spectra were then used in RBS to fit the spectra. Additionally, but without further explanation, LEEIXS (low-electron energy-induced X-ray spectrometry) and XPS were applied for the determination of the bonds between the atoms.

6.2 Elastic recoil detection analysis

Since the hydrogen content in silicon oxynitride films influences the physical properties, many authors try to gain some information on the hydrogen content in their films. The disturbing background of heavy elements (e.g. Si, Al, …) of RBS is absent in ERDA [149], and, therefore, this technique is described as more sensitive and reliable for monitoring small amounts of oxygen or thin oxidized layers. An ion beam of 30 MeV ^{28}Si atoms at a scattering angle of 35° and a 8.9-μm-thick Mylar absorber foil were utilized. With this method, the authors achieved the separation of the oxygen peaks resulting from the native oxide layer at the interface, the surface oxide layer, and the nitrogen peak in the oxidized silicon nitride films, but the films had to be kept thinner than 50 nm, otherwise oxygen and nitrogen peaks would have overlapped. The values observed by RBS and ERDA agreed well with differences in the calculated oxidized layer thickness (with silicon dioxide composition) being smaller than 4 nm. Also hydrogen contents and profiles were determined by ERDA since the NRA was too time-consuming for samples with a hydrogen content lower than 1 at%. For this application, 2 MeV He ions were applied as the primary ion beam, only protons were not stopped by the Mylar foil. At a grazing angle of 5°, a depth resolution of 10 nm was specified and the recoiled protons were detected at a scattering angle of 30°.

Also, [154] dealt with the determination of the hydrogen content in silicon oxynitride films. A $^{4}He^{+}$ ion beam with an energy of 2.4 MeV from a Van de Graaff accelerator was applied. The sample was tilted 15° to the beam position, and the recoiled protons were measured at an forward angle of 30° by a surface barrier detector while the He ions were stopped by an aluminum filter. A silicon sample implanted with hydrogen was used as a reference material. The dependence of the refractive index on the hydrogen concentration was given in a figure, but the overall composition in silicon, oxygen, and nitrogen of the samples was not specified. Hence, the effect shown by this graph supposedly was only partly produced by the hydrogen content and mainly by the change in the oxygen and nitrogen contents of the films.

Another application for ERDA was the investigation of deuterium diffusion in silicon oxynitride films annealed in a deuterium/nitrogen atmosphere, noting that ERDA was capable of distinguishing between hydrogen and deuterium [72]. The authors also state that IR was able to distinguish between the two isotopes. No further details on the origin of the O/(O+N) ratio and the film thickness determination were given. ERDA was used for the determination of quantitative hydrogen and deuterium depth profiles. Because of the film thickness in the range of 700–910 nm, ^{28}Si ions at an energy of 37 MeV were used and the incidence and recoil angle were 25° and 57.5°, respectively. The main conclusions were the increasing amount of incorporated hydrogen with increasing O/(O+N), the sum of the deu-

terium and hydrogen contents in the depth profiles was equivalent to the initial hydrogen depth profiles, and a structural rearrangement was stated because of the disappearance of Si–H bonds in the IR spectra. Diffusion coefficients were calculated. The exchange reaction energy for conversion of N–H and D_2 to N–D and HD was given as 1.5 eV and the diffusion rate was found to be lower in pre-annealed films. The same group of authors had already published a diffusion coefficient in [155] which showed a minimum in the range of O/N = 0.3.

ERDA spectra with a ^{35}Cl ion beam of 30 MeV were performed in [71], and the time-of-flight method was used for the discrimination of the masses of silicon, oxygen, and nitrogen. The hydrogen content was determined in an experiment including a Mylar absorber. A uniform concentration profile was found for all four elements. The amount of silicon dangling bonds was investigated by ESR. The films all showed a high amount of incorporated hydrogen. The data obtained were used to find a method for quantitative IR analysis of the films.

In [11] ERDA spectra were used for the quantification of SiO_XN_Y films and the oxygen, nitrogen, and hydrogen features were identifiable. The detection sensitivity for oxygen was given with 0.1 at%.

In [136], a PECVD film was analyzed by HFS and a hydrogen content of 34 at% was found; no further details on the analysis were specified. HFS with 2.28 MeV He ions were also performed in [151]. The incidence angle was 75° from the sample surface, the forward scattered hydrogen atoms were collected at 30° from the forward trajectory. He ions were eliminated by an aluminum foil.

6.3 Nuclear reaction analysis

High-resolution depth profiling of SiO_XN_Y films by narrow nuclear resonance reactions are investigated in [156]. A simulation program was used to convert the complex excitation curves into concentration profiles. Some assumptions were made, including that the density of the samples and the stopping power was the same as for silica or for Si_3N_4. NRA measurements were performed with a 2.5 MeV van de Graaff accelerator. The nuclear reactions $^{15}N(p,\alpha)^{12}C$ at 1 MeV, $^{16}O(d,p_0)^{17}O$ at 0.81 MeV and $^{18}O(d,\alpha)^{15}N$ at 0.73 MeV were used. The film thickness was calculated from the total amounts of nitrogen and oxygen by means of the density of a two-component mixture of SiO_2 and Si_3N_4. The difference to results obtained by ellipsometry was in the range of 15 %. Nuclear narrow resonance profiling was performed with protons, which lose their energy mainly due to inelastic collisions with the electrons of the light elements in the sample. The energy of the protons was tuned to the 152 or 429 keV resonance corresponding respectively to the reactions $^{18}O(p,\alpha\gamma)^{15}N$ and $^{15}N(p,\alpha\gamma)^{12}C$. The samples were also analyzed by AR-XPS.

The total γ-cross-section of the $^{14}N(d,p\gamma)^{15}N$ was determined in [157] over the deuteron energy range of 500–1500 keV with silicon nitride films on silicon substrate with a NaI(Tl) bore hole detector at the Dynamitron Tandem Laboratory in Bochum. Gamma ray energy of the nitrogen signal was found to be 7.3 and 8.3 MeV.

Analytic ion beam methods were used in the very detailed publication [158], because ultrathin films with thicknesses in the nm-range had to be investigated. The authors emphasize the advantages of these quantitative analytical methods over the alternative depth profiling techniques by sputtering, because the stabilization depth of at least 10 nm for the latter methods until equilibrium conditions are reached at the sputtered surface is too thick for ultrathin films or sharp interfaces. Even for thicker films, the depth resolution of SIMS is stated to be 3 nm. This argument of course is true only for dynamic SIMS with higher sputter rates. With this background, NRA was the main tool used in this publication, because of the high sensitivity and selectivity that could be achieved by this method. The total amounts of ^2H (D), ^{14}N, ^{15}N, ^{16}O, and ^{18}O were determined using the cross-section "plateaus" of the following reactions: $^2H(^3He,p)^4He$, $^{14}N(d,\alpha_0)^{12}C$, $^{15}N(p,\alpha\gamma)^{12}C$, $^{16}O(d,p_0)^{17}O$, and $^{18}O(p,\alpha)^{15}N$, the sensitivities of these reactions were given as 10^{12}–10^{14} atoms/cm^2. The resonance cross-section regions of the reactions $^1H(^{15}N,\alpha\gamma)^{12}C$, $^{15}N(p,\alpha\gamma)^{12}C$, $^{18}O(p,\alpha)^{15}N$, were also mentioned. The total amount of ^1H was

detected by the resonance given above or by ERDA. In ERDA, a tilting angle of the sample of 75° and a detection angle of 30° were used for the incident α particle beam of 2.2 MeV. The authors also excluded RBS as a valuable analytical method for this problem, since the high background of the silicon substrate prevented analysis of light elements. Only by applying channelling would this drawback have been avoided. Channelling was also used to resolve the signal from the silicon substrate and the silicon of the films by combination of 0.8–2 MeV α particles, channelling along one of the major crystalline axes of the underlying silicon substrate, and detection of the scattered α particles at grazing angle of 95–105° relative to the beam direction. In this way, an increase in sensitivity for light elements in the dielectric films was achieved and the average stoichiometry was measured. NRRA with the above given reactions was used for the depth profiling of silicon, oxygen, nitrogen, and hydrogen in the films. The small widths of these resonances (~100 eV), the high stopping power because of the low energies at which they occur, and the high-tilt geometry (70°) allowed a depth resolution of 1 nm to be accomplished with this nondestructive technique. Also, chemical etching of the films and successive NRA analysis was attempted culminating in a depth resolution of 0.5 nm. For the depth profiling of silicon deposited on silicon wafers with NRRA, the reactions $^{28}Si(p,\gamma)^{29}P$, $^{29}Si(p,\gamma)^{30}P$, and $^{30}Si(p,\gamma)^{31}P$ were mentioned. Even isotopic tracing of silicon was performed by depositing isotopically pure ^{29}Si. As further improvements for the analysis of ultrathin films, the authors also suggested complementing the ion beam analytical techniques with surface atomic methods such as LEED, RHEED, AES, XPS, UPS, IR, STM, and AFM. DIGME (deuteron-induced gamma-ray emission) was also attempted as a future potential candidate with the $^{16}O(d,p\gamma)^{17}O$ reaction.

As a third method in [149], NRA was employed to gain hydrogen depth profiles using the resonant nuclear reaction $^{1}H(^{15}N, \alpha\gamma)^{12}C$ at 6.39 MeV. The depth resolution was given as 5 nm, but the method turned out to be time-consuming for concentrations lower than 1 at%. Hydrogen depth profiles were obtained in [159] utilizing the same nuclear reaction. Oxidation and nitridation processes were investigated using also other analytical techniques not described in detail, such as ERDA, RBS, IR, AES, and TEM. Also in [139], this resonance technique was applied using ^{15}N atoms accelerated to 6.4–7.0 MeV in order to quantify the hydrogen content.

In [11] the detection sensitivity of oxygen for NRA was given with 0.1 at%, the same as for ERDA.

Nuclear reaction analysis was applied in [65] to determine hydrogen depth profiles of 50–100 nm thick films. LPCVD films showed concentrations of 2–4 at% and PECVD films had concentrations of 9–22 at% because of the lower substrate temperature. Silicon nitride films were shown to have generally more hydrogen than oxide and oxynitride films. The depth distribution of hydrogen showed a decrease of the amount of hydrogen near the interface. The difference in the hydrogen distribution was suggested as an explanation of the differences in etch rates, density, randomness in the film structure, and film stress.

NRA analysis in [73] was performed with a F^+ beam in order to determine the total hydrogen content in the SiO_XN_Y films as a function of deposition conditions.

The composition of films, which were produced without any obvious oxygen source, was determined by NRA as the N/Si ratio using (d,p) reactions in [26]. An anodically oxidized Ta_2O_5 film was used as the oxygen standard and the accuracy of the measurement as well as the nitrogen and silicon standard were determined by RBS. The authors describe the accuracy for the absolute value of N/Si as 6 %. Depth profiles of the films were obtained by AES measurements using a primary electron beam of 4 keV and 100 nA at a 200×200 μm^2. An area of 2×2 mm^2 was sputtered with 20 mA Ar ions with an energy of 2 keV. The interface abruptness was examined with this method without quantification. NRA was also used for the determination of silicon and nitrogen atomic densities and for the film density, with the film thickness values known from ellipsometric measurements. The absolute error for the density measurements is given as 4 %.

Nuclear microanalysis by observation of the backscattered particles and the nuclear reactions $^{16}O(d,p)O^*$ and $^{14}N(d,\alpha)^{12}C$ were investigated by comparison with reference targets together with RBS analysis in [160]. Also, FTIR transmission measurements were performed in the range of 400 to 4000 cm^{-1} for films deposited on silicon wafers.

NRA was used in [161] to determine the total ^{15}N, ^{16}O, and ^{18}O amount in the samples. The plateaus of the differential cross-section curves for the reactions $^{15}N(p,\alpha\gamma)^{12}C$ at 1 MeV, $^{16}O(d,p_0)^{17}O$ at 810 keV, and $^{18}O(p,\alpha_0)^{15}N$ at 730 keV. The authors of this article state that convenient standards were used. The film thickness was estimated by the results. Depth profiles were obtained by using the narrow nuclear resonance reactions $^{15}N(p,\alpha\gamma)^{12}C$ at 429 keV, $^{18}O(p,\alpha)^{15}N$ at 151 keV, and $^{29}Si(p,\gamma)^{30}P$ at 414 keV. The resolution of the depth profiles obtained is given as 1 nm near the film surface. Oxidation experiments were performed with ^{18}O-enriched gas. The same group of authors also used this method to perform isotopic tracing in [162].

The analysis performed for our working group started with the determination of nitrogen and oxygen by NRA with the nuclear reactions $^{16}O(d,p_0)^{17}O$ and $^{14}N(d,p_3)^{15}N$ by applying 1.1 MeV ^2H projectiles [84]. By the use of a calibration sample (TiN_XO_Y) quantitative data can be obtained since the peaks areas are proportional to the oxygen and nitrogen content of the films. The hydrogen content was determined by ERDA with 2.2 MeV He particles. The RBS results were obtained by sample bombardment with 2.2 MeV He particles. The evaluation of the NRA measurements were based on the assumption of a uniform distribution of the elements with depth and a constant nuclear reaction cross-section, which due to the sample thickness is not quite valid. The relative error of analysis was estimated by the experimentalist as 10–30 %. The results obtained were the contents of oxygen and nitrogen in the range of 10^{17} at/cm^2 without depth resolution. Also, in the second step for the determination of the hydrogen content by ERDA approximations had to be accepted since the evaluation of the hydrogen content was made in terms of $Si_{10}O_{20}H_X$. The concentration of hydrogen was found to be too low to affect the results obtained by RBS and was not further exploited. Only after the RBS analysis step, which included successive correction of the contents of oxygen, nitrogen, and hydrogen, were the results assumed to be definite [163–165]. Also the thickness of the samples was calculated assuming an atomic density of 6.6×10^{22} at/cm^3. Since too many assumptions were necessary for the quantification of these measurements and the high standard deviation was high, the results were only taken as tentative values for comparison in [118], but they were not used for any calibration.

For comparison, the samples were also analyzed at a second institute. Backscattering measurements were performed there with 2.199 MeV ^4He bombardment and 3.948 MeV ^4He bombardment. The samples were also analyzed at this facility by NRA in order to obtain information on the hydrogen content and in-depth distribution. At the higher energy, nuclear reactions also occur in competition to Rutherford backscattering, which allows better limits of determination for nitrogen [84]. In this case, the nuclear resonance reaction under investigation was $^1H(^{15}N,\alpha\gamma)^{12}C$ and the γ emission was determined. These experiments were performed by bombardment of the samples by nitrogen ions with 1 μA $^{15}N^{3+}$ up to 7.5 MeV and 150 nA $^{15}N^{4+}$ up to 9.5 MeV [166]. The hydrogen content of a small series of samples was evaluated thoroughly by NRA together with the density of the samples. The results are listed in Table 3. The depth distribution of hydrogen in all samples turned out to be very homogeneous [166]. A typical depth profile is given as intensity of the γ-ray emission vs. ^{15}N bombardment energy.

The results of the hydrogen quantification were used for the determination of the relative sensitivity function of hydrogen for SIMS, given in [34].

Ion beam analytical methods, especially RBS, are often called absolute methods not needing calibration. In case of oxynitride films with a thickness of >300 nm this assumption could not be proven. Because of the high uncertainties in the nuclear reaction cross sections and the necessity to assume certain unknown parameters, these methods also need to use standard materials for calibration. Otherwise, only semiquantitative results can be obtained. These methods can of course be useful for comparison with the results from other methods of analysis, and also for the determination of the relative sensitivity factors of hydrogen [34,118]. In all cases, the high error of analysis has to be kept in mind. As

stand-alone methods, these ion beam analytical techniques cannot be recommended due to the enormous instrumental cost, the troublesome evaluation, and the low accuracy for standardless analysis.

Table 3 Quantitative hydrogen results and density of six SiO_XN_Y films, obtained by NRA.

		EPMA		NRA	
Sample	Atom fraction Si/%	Atom fraction O/%	Atom fraction N/%	Atom fraction H/%	Density/g cm^{-3}
1	39.4 ± 0.4	6.7 ± 0.4	49.1 ± 0.3	4.7 ± 0.2	2.36 ± 0.12
2	42.5 ± 0.4	1.1 ± 0.1	54.8 ± 0.3	1.6 ± 0.1	2.45 ± 0.13
3	37.6 ± 0.4	9.0 ± 0.3	45.6 ± 0.4	7.8 ± 0.4	2.45 ± 0.13
4	34.4 ± 0.4	32.1 ± 0.3	24.7 ± 0.3	8.7 ± 0.4	2.30 ± 0.12
5	31.8 ± 0.3	54.2 ± 0.3	7.6 ± 0.4	6.4 ± 0.3	2.33 ± 0.12
6	37.0 ± 0.4	19.1 ± 0.3	37.7 ± 0.4	6.3 ± 0.3	2.24 ± 0.12

7. PHOTON ACTIVATION ANALYSIS

PAA usually uses electrons with an energy of 30 MeV, which are directed at a tantalum target and produce a beam of high-energy Bremsstrahlung. The sample is irradiated by this high-energy radiation and nuclear particles are ejected from the nucleus generating radioactive isotopic species (the nuclear photoeffect) [167]. Finally, the signal generated by the radioactive decay of the radioactive species is measured and analyzed.

No publications on PAA analysis of oxynitride films of aluminum and silicon were found in the literature by the authors. All PAA measurements by our working group were performed at the LINAC facility in Berlin. The exposure time was 300 s, the gamma measurements were started 404 s after the irradiation, and the measurement time was set to 120 s. The electron energy of the facility was tuned to 17 and 29.5 MeV, hence the maximum photon energy was also 17 MeV in one case and 29.5 MeV in the other.

For the determination of oxygen and nitrogen, the following reactions are applied usually and thus they were also used for quantification in our investigation:

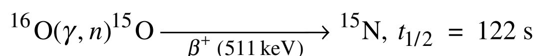

$$^{16}\mathrm{O}(\gamma, n)^{15}\mathrm{O} \xrightarrow[\beta^+ \text{ (511 keV)}]{} {}^{15}\mathrm{N},\ t_{1/2} = 122\ \mathrm{s}$$

$$^{14}\mathrm{N}(\gamma, n)^{13}\mathrm{N} \xrightarrow[\beta^+ \text{ (511 keV)}]{} {}^{13}\mathrm{C},\ t_{1/2} = 598\ \mathrm{s}$$

The β^+ radiation can only be measured indirectly by the annihilation radiation at 511 keV.

A disadvantage of this method is the identical energy of the resulting radiation for oxygen and nitrogen, consequently the two signals of oxygen and nitrogen can only be separated by the difference in the curve of radioactive decay due to the different periods of decay of ^{15}O and ^{13}N.

Additional to the two nuclear reactions for oxygen and nitrogen given above, other reactions also took place in SiO_XN_Y films deposited on silicon:

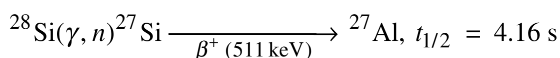

$$^{28}\mathrm{Si}(\gamma, n)^{27}\mathrm{Si} \xrightarrow[\beta^+ \text{ (511 keV)}]{} {}^{27}\mathrm{Al},\ t_{1/2} = 4.16\ \mathrm{s}$$

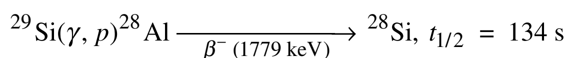

$$^{29}\mathrm{Si}(\gamma, p)^{28}\mathrm{Al} \xrightarrow[\beta^- \text{ (1779 keV)}]{} {}^{28}\mathrm{Si},\ t_{1/2} = 134\ \mathrm{s}$$

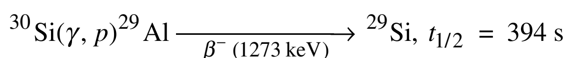

$$^{30}\mathrm{Si}(\gamma, p)^{29}\mathrm{Al} \xrightarrow[\beta^- \text{ (1273 keV)}]{} {}^{29}\mathrm{Si},\ t_{1/2} = 394\ \mathrm{s}$$

The first of these nuclear reactions, the ^{27}Si signal, has already decayed at the beginning of the measurement.

The nuclear reactions caused by exposure of elements to high-energy radiation are well known and for SiO_XN_Y and AlO_XN_Y films are already stated in literature. Unfortunately, it is that simple only as long as the single elements are concerned, but interactions between the elements are usually not known prior to analysis. In case of the oxygen determination, it turned out that the silicon matrix also provides a signal at 511 keV due to the pairing effect caused by the ^{28}Al decay to ^{28}Si at the decay rate of 134 s, which is too close to the decay rate of ^{15}O (122 s) to be separated. As a result, the oxygen content could not be determined by PAA.

This problem was less pronounced for nitrogen due to the much longer decay rate of the ^{13}N signal. Nonetheless, the nitrogen determination could not be started until the decay of the ^{28}Al had completed, which took about 15 min.

Finally, three SiO_XN_Y samples were analyzed and quantified. The PAA results gave the total mass of nitrogen in the entire analyzed sample. A comparison of PAA results with EPMA results is given in Table 4. The density given in this table was determined by NRA, and the film thickness was determined by SEM [166]. A general agreement between the results of the two methods is established, although the large error of the PAA results is a drawback.

Table 4 Comparison of the nitrogen results of PAA and EDS–EPMA.

	PAA		EPMA
Mass fraction N/μg	Density/g cm^{-3}	Weight fraction N/%	Weight fraction N/%
57 ± 6	2.45 ± 0.13	30.6 ± 6.1	38.7 ± 0.4
32 ± 4	2.24 ± 0.12	20.7 ± 4.6	18.9 ± 0.3
49 ± 6	2.30 ± 0.12	31.3 ± 6.9	28.2 ± 0.3

8. SPUTTERING TECHNIQUES

This group of analytical techniques is applied especially in cases of nonuniform distribution of the elements with depth or if the interfaces are of special interest. Depth profiles can be recorded with different resolution, depending on the method used and the sputter rate. The sputtering applied in these techniques is not only necessary for the successive removal of the sample surface as in AES, but it is necessary for signal generation. Therefore, sputtering techniques can only be performed in a destructive way.

8.1 Secondary ion mass spectrometry

This very sophisticated method is relatively often mentioned in the literature, probably because it is one of the oldest sputtering techniques in analytical chemistry. However, usually the authors do not give any details on the instrument used, the analytical parameters, or the quantification procedures [92,93]. Sometimes the interpretation of SIMS depth profiles is attempted without considering the background pressure and the changes of sputtering rate at interfaces [168]. Quantification of stoichiometric SiO_XN_Y and AlO_XN_Y films with SIMS is especially difficult since the films are electrically insulating. As a result, information on the exact quantification procedures and the way sample charging is avoided is crucial for comprehensive information.

An advantage of SIMS is the possibility to obtain the hydrogen distribution in the film. SIMS profiles of SiO_XN_Y films showing low oxygen and hydrogen contents were determined in [169,170]. The films were in the range of several tens of nm, deposited on silicon wafers. The depth profiles were given as intensity vs. depth diagrams. Quantification was not attempted; only the qualitative depth distribution of silicon, oxygen, nitrogen, and hydrogen in mono- and multi-layered structures was of interest. Furthermore, the position of the main stretching vibrational mode of the IR spectra and the full width at half maximum were listed with the deposition conditions in [169], while a detailed description of the

excimer laser-induced deposition was given in [170]. The composition of the films was not quantified in these publications.

A PHI Trift II TOF-SIMS instrument was used in [94] with a 15 keV Ga^+ beam for data acquisition and a 1 keV Cs^+ beam for sputtering. Also in this publication, the intensity vs. depth profile of only one ca. 10 nm thick film is given.

Cesium molecular ions were used in [171] to achieve depth profiles of oxygen and nitrogen without further information on the quantification procedure, except that with CsM^+ the sensitivity for all elements was stated to be relatively uniform [172]. This, of course, is not valid and was disproved in [84].

In [173], cesium was used for sputtering and the secondary ion counts of silicon and nitrogen or silicon and oxygen were utilized. The authors did not quantify the data due to the lack of standard samples to correct the matrix effect, but used only the secondary ion counts to determine the nitrogen distribution.

SIMS can also be utilized for the analysis of other elements, especially trace elements, in films and bulk material. SiO_XN_Y films are effective as dielectrics in scaled CMOS (complementary metal oxide semiconductor) structures for the prevention of boron diffusion. Quantitative AES depth profiles of nitrogen and SIMS depth profiles of boron were shown in [174], also without further information on the analytical procedure.

SiO_XN_Y films were also investigated as Zn diffusion barriers. SIMS depth profiles of oxynitride films deposited on GaAs with 150 nm thickness are shown in [175] and the isotopes ^{66}Zn and ^{64}Zn were registered as well as the silicon signal for definition of the interface. The results were given in the intensity vs. cycle diagrams. Also in this case, quantitative analysis was not performed by SIMS, but by AES. The oxidized sample surface was removed by Ar ion milling, and the measurements were carried out with 5 keV accelerating voltage and a voltage of 5×10^{-7}A. The ratio of the (KLL) differential signal intensities of silicon, nitrogen, and oxygen were used to precisely determine the atomic fraction of oxygen and nitrogen in the film. The composition was finally estimated with the help of relative sensitivity factors and given in the representation of O/(O+N). The origin of the relative sensitivity factor was not further stressed. The same group of authors has also published their results with a little more emphasis on the correlation between the refractive index obtained by ellipsometry measurements at 632.8 nm and other properties in [12].

1 keV Xe ions were used for SIMS measurements with a Perkin–Elmer PHI SIMS II system in [173]. The samples were charge-compensated with a 2 keV electron beam. Si_2X^+ molecular ions (X = e.g., O, N, …) were detected and the sensitivity factors were calculated from quantitative AES measurements also given in this publication. Laboratory standard samples, which were not further specified, were used for calibration.

The advantage of the enormous range of several orders of magnitude of compositions that can be measured by SIMS was exploited in [151]. A PHI 6650 quadrupole SIMS instrument with 2.0 keV Cs^+ ions was used and the cesium molecular ions of silicon, oxygen, nitrogen, and hydrogen were measured. The sputter rate was determined by profilometry. The SIMS depth profiles were calibrated by RBS/HFS results. The films had a thickness of about 30 nm, and the minimum measurable thickness was given as 10 nm.

No details on the measurement are given in [177], and the authors of the paper state that the SIMS ion counts were converted into the nitrogen density by using one standard SiO_XN_Y sample provided by Evans East. The strong matrix effect of the oxygen content of the films was not taken into consideration. SIMS measurements were performed in [177] on a CAMECA IMS 3f double focusing instrument using Cs^+ primary ions with a primary ion energy of 5.5 keV and a primary ion current of 10 nA. The sputtered area was 400×400 μm^2, whereas the diameter of the analyzed area was 60 μm. Since quantitative analytical results were needed, depth profiles were recorded.

The analytical procedure, handling of the sample charging, and the quantification by atomic ions, molecular ions, and cesium molecular ions are described in detail in the [34,81]. It was shown in those publications that cesium molecular ions are the best choice for the quantitative depth profiling of oxy-

nitride films in comparison to atomic ions and silicon or aluminum molecular ions. By the use of reference samples quantified by EDS-EPMA, it was possible to derive the equations for the calculation of the relative sensitivity factors. The relative sensitivity factors of oxygen and nitrogen vary with the composition of the films due to the matrix effect. However, solving the respective set of equations enables the quantitative depth profiling of unknown graded films and films with inhomogeneous depth distribution. In combination with NRA, it was possible to determine the relative sensitivity function for hydrogen, which is shown in [34].

Consequently, SIMS is the only analytical technique that allows the quantitative depth analysis of hydrogen with high depth resolution. The drawback of the matrix dependence of the signals can be overcome by the use of the evaluated relative sensitivity functions. Therefore, no further standards are necessary for quantification of such films with SIMS, if the applicability of the relative sensitivity functions at other instruments is confirmed by the evaluation of one reference sample with known composition.

8.2 High-frequency, secondary neutral mass spectrometry

No literature on the analysis of SiO_XN_Y and AlO_XN_Y films using this method of analysis was found by the authors.

The measurements performed for our working group were carried out with a Leybold INA 3 electron gas SNMS instrument. The argon gas (>5 N purity) pressure was set to 0.3 Pa. The residual gas pressure in the plasma chamber was 0.5×10^{-6} Pa. The frequency of the voltage (500 V) was set to 200 kHz with a sputter period of 80 %, while the plasma frequency was 27.16 MHz. The sputtered area was 3 mm in diameter for all measurements. The post-ionized intensities of the N^0, O^0, Al^0, AlH^0, Si^0, and SiH^0 secondary neutrals were measured.

Sample charging is avoided in the high-frequency operation mode of SNMS, working with a high-frequency argon plasma. An additional square-wave high-frequency voltage is applied to the sample. During the positive half-wave of the applied hf-voltage, a short electron pulse is applied to the surface for the compensation of the positive charge caused by the preceding ion bombardment interval.

Measurements performed using SNMS on oxynitride films revealed a surprisingly strong matrix effect, contrary to the general opinion that no such effects are shown. The observed effect was much weaker than that encountered in SIMS. Details are given in [34,81]. This effect was based on the atypical composition of the samples with a very wide concentration range of oxygen and nitrogen, and on the influence of the sputtered oxygen on the plasma conditions, which became obvious by the performed measurements. Evidently, the oxygen sputtered from the sample surface influenced the ionization probabilities of the other matrix components by changing the plasma conditions, especially since the dwell time of the sputtered particles in the plasma was rather long.

Because of the plasma, no high vacuum conditions were possible, and hence the detection limits for oxygen, nitrogen, and hydrogen determined in [34,81] were in the range of a few at%. Results of this and similar studies have triggered the development of a new generation of SNMS instruments with improved vacuum system and chamber geometry. With these instrumental developments, the detection limits were improved by one order of magnitude, which is described in [34].

8.3 High-frequency, glow discharge optical emission spectrometry

No publications on the analysis of SiO_XN_Y and AlO_XN_Y films with this method were found by the authors of this article.

Our working group applied a LECO GDS 750 spectrometer equipped with a GRIMM-type source with a 4-mm-diameter anode. The instrument used in this study was modified by a new free-running hf-generator including the glow discharge source as a part of the oscillation circuit, which is powered

by a free-running rf-generator [178]. The argon plasma was operated at a pressure of 770 Pa and an effective rf-voltage of 550 V.

As the measurements of oxynitride films showed, similar to other methods, in hf-GDOES the amount of oxygen in the plasma, introduced by the sputtering of the films strongly influences the plasma conditions and therefore also the intensities of the other elemental signals. This is clearly demonstrated in [34,81], where also the quantification procedure of the obtained depth profiles is described. For the evaluation of the results in these two publications, the intensities of silicon, oxygen, and nitrogen were normalized with respect to the silicon nitride and silicon dioxide composition allowing a direct comparison of the matrix dependence of the emission intensity at different sample compositions. Since the normalized intensity of the nitrogen emission line did not change with sample composition, nitrogen can be quantified directly from the measured N/Ar-intensity using only one calibration sample. Silicon can be quantified with a linear calibration between the SiO_2 and Si_3N_4 calibration samples. Due to the high background, oxygen can only be quantified for concentrations higher than 20 at%, otherwise it has to be calculated from the difference to 100 %.

Although GDOES proved to be the fastest possibility for depth profiling, the high oxygen background limits the analytical capabilities to a great extent. Furthermore, hydrogen cannot be determined.

In [34], a useful side effect of this technique is exploited. Since optical emissions are recorded, interference patterns are part of the signal obtained during sputtering and are measured by the optical detectors. The interference effect is caused by the optically transparent films on the reflective silicon substrate and can be used for a rough estimation of the refractive index of the films.

9. MECHANICAL TECHNIQUES

9.1 Stylus measurement

Stylus measurements are often used to determine the depth of sputtering craters and profiles of a surface. If authors want to check the ellipsometry results for the film thickness, stylus profiles can be helpful. In case of [11], they were performed on wet-etched steps. Steps produced by shadowing a part of the substrate were applied in [68] together with optical interference for film thickness determination. The variation in the film thickness can also be determined this way; in [121], many spikes were observed on the rough surface of the films. The stress of SiO_XN_Y films was calculated from the curvature of coated Si(100) wafers, which can be measured by profilometry [99,136,176]. This allows the evaluation of the average stress throughout the whole film. The residual stress values given in [179] vary from –110 MPa to –390 MPa with increasing refractive index with a standard deviation of 15 %. The values obtained in [99] range from approximately +200 MPa tensile stress to –900 MPa compressive stress with increasing film thickness.

9.2 Atomic force microscopy

AFM measurements of the surfaces of films produced by pulsed laser deposition are shown in [20,52]. The surface morphology of SiO_XN_Y films at Si(100) substrates was examined with the TopoMetrix TMX 2000 atomic force microscope and show a strong dependence of the formation of islands on the substrate temperature.

The surface morphology and roughness of films was observed by AFM in air in [160]. The positive effect of hydrogen on the surface roughness of PECVD-deposited films is demonstrated by AFM images.

9.3 Hardness and elastic constants determination

The stability of materials and composites at elevated temperatures can be important for the durability of multilayer structures, for interface coatings for improvement of the fracture strength, and for protective coatings. Three single crystal materials, Si(100), sapphire, and hydrothermal quartz, were used as substrate material for the deposition of SiO_XN_Y films in [139]. The substrates for the cantilever beam measurements were rectangular, and the curvature and flatness were measured prior to and after deposition and annealing cycles. With the knowledge of the thermal expansion coefficient, the Young's modulus, and the Poisson's ratio of the substrate, the properties of the film, namely, biaxial modulus and intrinsic and thermal stress, were determined. The annealing had to be performed carefully, because otherwise cracking and hydrogen release at temperatures above deposition temperature with subsequent blister formation were observed for some films. The hydrogen content of the films was between 12 and 38 at%. The biaxial modulus of the films as deposited was in the range of 21–32 Gpa, and the biaxial intrinsic stress was tensile and <100 MPa. Annealing was performed in air, and a difference was observed between films deposited with mostly ammonia and with mostly nitrous oxide. While the first ones showed a loss of nitrogen in form of $–NH_X$ species and an increase of the biaxial modulus to 80 GPa and of the intrinsic stress to 500 MPa, the second had a lower hydrogen content and higher temperatures were needed to release nitrogen. These films were transformed to the oxide at temperatures of 350–400 °C and the biaxial modulus increased to ~100 GPa, the intrinsic stress to 200–250 MPa, but the films did not crack up to temperatures of 450 °C. The SiO_2 formation resulted from the loss of nitrogen and hydrogen and from inward diffusion of oxygen. The time needed for oxygen to diffuse through a 1-μm SiO_2 film at 350 °C was specified as 28 h.

Ultra-microindentation was performed in [180] with a Berkovich triangular base diamond pyramid indenter and the principles of the method were explained. Hardness and Young's modulus results for various oxide, nitride, and oxynitride films were also given. The instrument used had a force resolution of 10 mN and a depth resolution of 10 nm and was less sensitive than the nano-indenter.

Continuous microindentation with a Fischerskope H100 using a Vickers indenter with 25 mN load was performed in [181] on magnetron-sputtered AlO_XN_Y films. The films deposited at higher temperatures showed a pitted surface in SEM and crystallinity in XRD. The plastic hardness was in the range of 8 to 38 GPa, the universal hardness 4 to 8 GPa, the elastic modulus 80 to 190 GPa.

Microindentation curves on 4-μm-thick films with a maximum load of 10 mN were performed in [182]. A diamond pyramidal Vickers indenter was used, and load and penetration were recorded during indentation. An example is shown together with the formulas used for the calculation of hardness and elastic modulus. The maximum indentation depth was found to be 0.42 μm. The authors state that, since no modification of the slope of the loading curve is observed, single film behavior and thus also no substrate influence is encountered. The hardness is given with 9 GPa, the elastic modulus with 34 GPa. The elastic recovery of the silicon oxynitride films deposited on PVC substrates was 85 %.

Young's modulus and Poisson's ratio of 5 X-ray amorphous AlO_XN_Y films were determined in [43] by a cantilever beam vibration method. The film was deposited on a stainless steel substrate, and the resonance frequencies of the substrate and the coated substrate were measured. The Young's modulus and Poisson's ratio were obtained by measuring wide and narrow substrates. The dynamic hardness of the films deposited on slide glass was measured with a dynamic ultra micro hardness tester (Shimadzu, DUH-50), which records the penetration depth of the indenter during loading. A maximum load of 49 mN and a maximum loading rate of 0.47 mN/s were applied. Diagrams giving the measured property vs. AlN content were shown. The Poisson's ratio decreased monotonically with the AlN content (approximately 0.22 at 0 mol% - 0.19 at 80 mol% AlN), the Young's modulus decreased with increasing AlN content up to 50 mol% AlN, then the correlation inverted (approximately 122 GPa at 0 and 80 mol% and 100 GPa at 50 mol%). The dynamic hardness was presented vs. penetration depth and was strongly dependent on the depth (i.e., load). The dynamic hardness at the depth of 3 μm was also given vs. the AlN content with an accuracy of ±8 %. Again, a decrease with increasing AlN con-

tent up to 50 mol% AlN was observed and an increase beyond this composition (approximately 620 kg mm^{-2} at 0 and 80 mol% and 520 kg mm^{-2} at 50 mol%). These results were explained by the authors by assuming that there was a decrease of higher sixfold-coordinated aluminum atoms for AlN contents <50 mol%. Above this composition, the lower fourfold-coordinated state remained, but the nitrogen was substituted by oxygen and the Young's modulus increased as expected.

9.4 Nano-indentation

An ultra-microindenter (NHT by CSEM) with a Vickers diamond was used in [179] to determine the film hardness of SiO_XN_Y films. The average value of five indents performed with 1–100 mN maximum load was calculated. The loading/unloading cycles of this instrument are given in indentation depth, which is measured differentially, vs. load. The hardness of the films was found to be independent of the load up to a penetration depth of approximately 30% of the film thickness, which was in the range of 700 nm. Mostly, multilayered film structures were evaluated and the values for continuously varying films and films with abrupt interfaces were compared. The hardness values varied not continuously from 7.5 to 13.5 GPa with increasing nitrogen content. The Young's modulus was 114–135 GPa. The composition of the films was not determined.

Nano-indentation measurements were performed with a Hysitron Triboscope with AFM on SiO_XN_Y films with 100-nm thickness deposited on glass [99]. The indents were taken with a load of 100 μN. The hardness seems to increase with process temperature in the IBAD system. The values ranged from 18 to 25 GPa.

Hardness and Young's modulus were evaluated by our working group by measurements with the Nano Hardness Tester (NHT) utilizing a Berkovich diamond tip (triangular). This instrument was commercialized by CSEM Instruments (Switzerland) [183] for indentation of thin films utilizing a differential capacitive measurement technique. A maximum load of 5 mN and a loading rate of 10 mN per minute were chosen for the measurements. The data obtained by the evaluation of the force vs. depth profiles of three loading/unloading cycles at different places of each sample were averaged and only the resulting mean was used.

An AFM is integrated in the instrument allowing high-resolution imaging of the film surface before and after the indent. This assures that every indentation measurement is performed at a flat surface region. For the image displayed in [31], the indent was carried out with 50 mN maximum load and with a loading rate of 100 mN per minute, showing that even at such a high load and resulting indentation depth no cracks occur in the film.

The indentation measurements are described in detail in [31]. The relative standard deviation of the hardness value was 3.7 % and for the Young's modulus 1.2 %, indicating the excellent reproducibility of the hardness tester.

One problem arises when the hardness of films is tested, and this is the influence of the substrate on the indentation measurements. The hardness values obtained are dependent on the film hardness alone only if the indents are shallow enough compared to the film thickness. Therefore, the film thickness, representing any possible emerging influence of the substrate on the hardness results, was included into the statistical models. Unfortunately, for both hardness and Young's modulus, the film thickness turned out to be a significant term in the model describing the influences on these physical properties. Since the film thickness obviously was too low for excluding influences of the substrate even on the nano-indentation measurements, regression analysis was the only way to calculate the dependence of the hardness values of the thin films on the oxygen concentration and to exclude the influence of the film thickness on the results by sophisticated statistical means. The precise evaluation of the nano-indentation measurements is given in [31]. The ultra-microindentation measurements of [180] reveal very similar hardness and Young's modulus values to those obtained in our work. The hardness and Young's modulus values of [43] are of the same order of magnitude as those obtained by the measure-

ments performed in [31], but the correlation to film composition was inconclusive due to the low number of samples.

9.5 Tribological testing

The mechanical strength of SiO_XN_Y films was tested in [179] by low-load microscratch testing. The sliding speed was 0.5 mm s^{-1}. The load increased from 0.1–64 mN with a loading rate of 8 mN s^{-1}. The scratch tracks were evaluated by metallographic microscopy and also in three dimensions by AFM. Several AFM micrographs are given. The films were deposited on silicon, and the critical load for multilayer films with abrupt interfaces was, at 23 mN, slightly better than for graded films with 18 mN. The damage seemed to be produced by cutting.

A nanotribometer was used in [181], which is described as an instrument based on AFM technology. The position of the sample is determined by optical interference. A sapphire sphere with a diameter of 1 mm and a roughness of 4 nm was used. The tests were performed with a speed of 36 μm s^{-1} and a length of 30 μm. A Normarsky microscope was used for the detection of the wear effect, but AFM was used for imaging. The results for aluminum oxynitride films with an oxygen content of 3 to 62 at% show friction coefficients of 0.18 to 0.48, although the results vary widely. RHEED measurements were performed and revealed amorphous films or films with an AlN-like wurtzite structure.

The scratch tests in [75] were used to investigate the dynamic behavior of the silicon oxynitride films on PVC substrataes and the interaction forces by morphological evaluation of the scratches with SEM. A Berkovic indenter with a 120° trigonal-base pyramid was drawn edge forward with a controlled penetration depth, while a piezoelectric sensor recorded the interaction forces. The specific abrasion energy of the films at a penetration depth slightly higher than the film thickness is given with 2.3 N μm^{-2}.

9.6 Adhesion testing

A tensile pull-off tester was used in [99] to evaluate the adhesion of the SiO_XN_Y films on glass substrate. Values in the range of 80 Pa were achieved by the IBAD method for films with thicknesses from 0.1 to 0.7 μm.

10. SPECIAL METHODS

10.1 Hot gas extraction

The oxygen and nitrogen content of AlO_XN_Y films prepared by reactive rf-sputtering were determined by an inert gas fusion method with a Horiba EMGA-650 instrument in [43]. The samples were fused in carbon crucibles under helium gas and were quantitatively converted into CO and N_2. While CO was further oxidized to CO_2 and detected by IR absorption, N_2 was detected by a thermal conductivity detector. Although inert gas fusion is a valuable method for the determination of oxygen and nitrogen, the application for thin film analysis gives very inaccurate results. The weight of the substrate exceeds the weight of the film by orders of magnitude resulting in a large error. Accurate results by this method can be obtained only if the film is separated from the substrate prior to analysis, a procedure that is very difficult for film thicknesses less than 1 μm.

10.2 Weighing

The film thickness and the evaporation rate were determined in [38] by the frequency shift of a quartz oscillator and by scratching the film from the substrate and measuring the obtained mass. For all samples, a specific mass of 2 g/cm^3 was assumed.

TGA was used for the interpretation of annealing studies in [136] in order to evaluate any change of the weight during annealing.

10.3 Sink-float method

The density of five AlO_XN_Y films was determined in [43] by stripping the film from the copper plate and placing it in solutions chosen not to sink or to float the sample. The density of the solution which fulfilled this requirement was then measured by the Archimedes' method. The density decreased linearly from ~3.25 g/cm^3 for 0 mol% AlN to ~2.51 g/cm^3 for 80 mol% AlN. The accuracy is specified as ±0.1 %.

11. CONCLUSIONS

After reviewing all analytical methods, it has to be concluded that a critical evaluation is mandatory for each specific task and that it is very unlikely that accurate and reliable results can be achieved without reference samples. The limitations are manifold and have to be considered for each technique.

Most of the quantitative results published in the literature were based on electron beam analytical techniques, especially on AES, which is considered to be a technique with well-known relative sensitivity factors. Therefore the majority of the authors try to apply this analytical method under the wrong assumption that no calibration is necessary. Since most of the ternary or multicomponent metal–boron–carbon–oxynitride systems or films are metastable, electron beam techniques are apt to cause radiation damage in addition to charging. If sputter depth profiling is utilized in combination with AES, changes in the surface composition due to preferential sputtering also have to be considered. As a consequence, AES analysis of light components in insulating films is possible only for samples with compositions close to the composition of the calibration sample.

Ion beam techniques, which are often applied as absolute methods, deliver reliable results only if the film thickness is in the range used for microelectronic applications, which normally is less than 100 nm. For films with a thickness of more than 300 nm, which are common in the rapidly growing fields of large area coating, hard coating, and decorative coating, even particle beam techniques have to be calibrated by the use of reference samples. Otherwise, a rapid decrease in accuracy with increasing film thickness will be encountered.

In the case of sputtering techniques such as SIMS, SNMS, and GDOES, matrix effects are often neglected by the authors when quantifying depth profiles even for SIMS, where such effects are common knowledge. However, the results of our working group clearly demonstrate the matrix effects also for SNMS and GDOES in case of oxygen-containing films.

When we recapitulate the experiences made with the different methods of analysis, the following set of analytical methods is recommended. FTIR and EDS-EPMA are both quick and nondestructive methods for the determination of the bulk film composition. The film thickness can easily be determined by FTIR, while for EPMA the density must be known. EPMA can be used for film thicknesses down to 20 nm. It shows the best precision for concentrations higher than 5 wt% with excellent long-term repeatability, is matrix-independent, and allows lateral distribution analysis. The more expensive particle beam techniques like ERDA, NRA, and RBS can be recommended for thin films of less than 100 nm and for the confirmation of EPMA results for reference samples. Film samples may be destroyed under the high impact energy of the ion beams.

SIMS and hf-SNMS techniques are destructive methods of analysis for depth profiling, but only with SIMS is 3-dimensional analysis possible. Moreover, dynamic SIMS is the most precise method of analysis for concentrations lower than 5 wt% and it allows quantitative analysis of graded and multilayer films down to 10 nm thickness. Furthermore, SIMS is the only sputter method capable of hydrogen quantification. Hf-SNMS has the advantage of linear calibration, but oxygen can be quantified only for concentrations higher than 5 wt%. Hf-GDOES has the highest sputter rate, but is only practicable

as a semi-quantitative method. For a comprehensive characterization, additional methods are recommended. The determination of the film thickness gives the best results using a combination of the complementary methods of SEM and ellipsometry. From the ellipsometry measurements the refractive index can also be obtained easily. Hardness and Young's modulus can be determined by nano-indentation. XRD combined with modern tools for data evaluation is suitable for the investigation of crystallinity, crystal size, stress, microstrain, and texture in the films [185].

This recommended set of analytical techniques has meanwhile been successfully applied to numerous multicomponent systems such as CrON [185], CrMoON, CrVON, TiAlN, TiCON, TiAlCON, TiAlYON, and BCN [186].

12. REFERENCES

1. N. Shibata. *Jpn. J. Appl. Phys.* **34** (1), 4024 (1995).
2. F. H. P. M. Habraken, J. B. Oude Elferink, W. M. Arnold Bik, W. F. Van der Weg, A. E. T. Kuiper, J. Remmerie, H. E. Maes, M. Heyns, R. F. De Keersmaecker. *LPCVD Silicon Nitride Oxynitride Films*, F. H. P. M. Habraken (Ed.), Chap. 1, Springer, Berlin (1991).
3. F. H. P. M. Habraken and A. E. T. Kuiper. *Mater. Sci. Eng.* **R12**, 123 (1994).
4. H. J. Stein. *Proc. Electrochem. Soc.* **89-7** (Proc. Symp. Silicon Nitride Silicon Dioxide Thin Insul. Films, 1988) 3 (1989).
5. J. Aarnio, P. Heimala, M. del Giudice, F. Bruno. *Electron. Lett.* **27** (25), 2317 (1991).
6. T. M. del Giudice, F. Bruno, T. Cicinelli, M. Valli. *Appl. Opt.* **29** (24), 3489 (1990).
7. T. Ogawa, M. Kimura, T. Gotyo, Y. Tomo, T. Tsumori. *Proc. Soc. Photo-Opt. Instrum. Eng.* (SPIE) - International Society for Optical Engineering, **1927/1** (Optical/Laser Microlithography VI) 263 (1993).
8. T. Ogawa, H. Nakano, T. Gocho, T. Tsumori. *Proc. Soc. Photo-Opt. Instrum. Eng.* (SPIE) - International Society for Optical Engineering **2197**, 722 (1994).
9. J. A. Underhill, V. S. Nguyen, M. Kerbaugh, D. Sundling. *Proc. Soc. Photo-Opt. Instrum. Eng.* (SPIE) - International Society for Optical Engineering **539**, 83 (1985).
10. D. V. Tsu, G. Lucovsky, M. J. Mantini, S. S. Chao. *J. Vac. Sci. Technol. A* **5** (4), 1998 (1987).
11. S. P. Speakman, P. M. Read, A. Kiermasz. *IPAT 87*, 6th International Conference on Ion and Plasma Assisted Techniques, 273 (1987).
12. A. Hashimoto, M. Kobayashi, T. Kamijoh, H. Takano, M. Sakuta. *J. Electrochem. Soc.* **133** (7), 1464 (1986).
13. D. Peters, K. Fischer, J. Müller. *Sens. Actuators A* **25–27**, 425 (1991).
14. M. J. Rand and J. F. Roberts. *J. Electrochem. Soc.* **120** (3), 446 (1973).
15. D. M. Diatezua, P. A. Thiry, R. Caudano. *J. Vac. Sci. Technol. A* **13** (4), 2099 (1995).
16. P. G. Snyder, Y.-M. Xiong, J. A. Woollam, G. A. Al-Jumaily, F. J. Gagliardi. *J. Vac. Sci. Technol. A* **10** (4), 1462 (1992).
17. Y.-M. Xiong, P. G. Snyder, J. A. Woollam, G. A. Al-Jumaily, F. J. Gagliardi, L. J. Mizerka. *Surf. Int. Anal.* **18**, 124 (1992).
18. G. A. Al-Jumaily, T. A. Mooney, W. A. Spurgeon, H. M. Dauplaise. *Mater. Res. Soc. Symp. Proc.* **128**, 61 (1989).
19. R. P. Howson and G. W. Hall. Private communications.
20. R.-F. Xiao, L. C. Ng, H. B. Liao. *Mater. Res. Soc. Symp. Proc.* **388**, 115 (1995).
21. A. E. T. Kuiper, S. W. Koo, F. H. P. M. Habraken, Y. Tamminga. *J. Vac. Sci. Technol. B* **1** (1), 62 (1983).
22. A. E. T. Kuiper, F. H. P. M. Habraken, A. van Oostrom, Y. Tamminga. *Philips J. Res.* **38**, 1 (1983).
23. S. K. Ghosh and T. K. Hatwar. *Thin Solid Films* **166**, 359 (1988).
24. S. V. Hattangady, H. Niimi, G. Lucovsky. *J. Vac. Sci. Technol. A* **14** (6), 3017 (1996).
25. J. Vuillod. *Proc. Electrochem. Soc.* **90-14** (Proc. Symp. Plasma Process., 8th, 1990), 605 (1990).

26. T. Carriere, B. Agius, I. Vickridge, J. Siejka, P. Alnot. *J. Electrochem. Soc.* **137** (5), 1582 (1990).
27. P. V. Bulkin, P. L. Swart, B. M. Lacquet. *J. Non-Cryst. Solids* **187**, 403 (1995).
28. R. Machorro, G. Soto, E. C. Samano, L. Cota-Araiza. *Mater. Res. Soc. Symp. Proc.* **526**, 97–102 (1998).
29. H. Birey, S.-J. Pak, J. R. Sites, J. F. Wager. *J. Vac. Sci. Technol.* **16** (6), 2086 (1979).
30. M. Xu and T.-M. Ko. *J. Vac. Sci. Techn. B* **18** (1), 127–135 (2000).
31. S. Dreer, R. Krismer, P. Wilhartitz, G. Friedbacher. *Thin Solid Films* **354**, 43 (1999).
32. A. Borghesi, E. Bellandi, G. Guizzetti, A. Sassella, S. Rojas, L. Zanotti. *J. Appl. Phys. B* **56**, 147 (1993).
33. S. Dreer, R. Krismer, P. Wilhartitz. *Surf. Coat. Technol.* **114**, 29 (1999).
34. S. Dreer, P. Wilhartitz, K. Piplits, H. Hutter, M. Kopnarski, G. Friedbacher. *Mikrochim. Acta* **133**, 75 (2000).
35. R. Swanepol. *J. Phys. Eng.: Sci. Instr.* **16**, 1214 (1983).
36. I. Ohlídal and K. Navrátil. *Thin Solid Films* **156**, 181 (1988).
37. W. Lechner. Ph.D. thesis, Optische Charakterisierung von dünnen dielektrischen Schichten abgeschieden mit PVD-Verfahren, University of Innsbruck (1999).
38. L. Kubler, R. Haug, F. Ringeisen, A. Jaegle. *J. Non-Cryst. Solids* **54**, 27 (1983).
39. D. Schalch, A. Scharmann, R. Wolfrat. *Thin Solid Films* **124** (3–4), 301 (1985).
40. S. Mirsch and J. Bauer. *Phys. Stat. Sol. A* **26**, 579 (1974).
41. S. J. Holmes and V. W. Biricik. *36th Annu. Technol. Conf. Proc - Soc. Vac. Coaters* 146 (1993).
42. G. A. Al-Jumaily, T. A. Mooney, W. A. Spurgeon, H. M. Dauplaise. *J. Vac. Sci. Technol. A* **7** (3), 2280 (1989).
43. T. Hanada, M. Kobayashi, S. Tanabe, N. Soga. *J. Non-Cryst. Solids* **135**, 227 (1991).
44. H. Demiryont, L. R. Thompson, G. J. Collins. *Appl. Opt.* **25** (8), 1311 (1986).
45. H. Demiryont, L. R. Thompson, G. J. Collins. *J. Appl. Phys.* **59** (9), 3235 (1986).
46. J. D. Targove, L. J. Ling, J. P. Lehan, Ch. K. Hwangbo, H. A. Macleod, J. A. Leavitt, L. C. McIntyre, Jr. *Mater. Res. Soc. Symp. Proc.* **93**, 311 (1987).
47. Ch. K. Hwangbo, L. J. Lingg, J. P. Lehan, H. A. Macleod, F. Suits. *Appl. Opt.* **28** (14), 2779 (1989).
48. B. G. Bovard. *Thin Solid Films* **206**, 224 (1991).
49. J. W. Osenbach and W. R. Knolle. *J. Electrochem. Soc.* **139** (11), 3346 (1992).
50. M. Vogt and R. Hauptmann. *Surf. Coat. Technol.* **74–75**, 676 (1995).
51. J. Olivares-Roza, O. Sánchez, J. M. Albella. *J. Vac. Sci. Technol. A* **16** (5), 2757–2761 (1998).
52. R.-F. Xiao, L. C. Ng, Ch. Jiang, Z. Yang, G. K. L. Wong. *Thin Solid Films* **260**, 10 (1995).
53. Y. Cros, N. Jaffrezic-Renault, J. M. Chovelon, J. J. Fombon. *J. Electrochem. Soc.* **139** (2), 507 (1992).
54. G. Lucovsky and D. V. Tsu. *J. Vac. Sci. Technol. A* **5** (4), 2231 (1987).
55. E. Fogarassy, C. Fuchs, A. Slaoui, S. de Unamuno, J. P. Stoquert. *J. Appl. Phys.* **76** (5), 2612 (1994).
56. P. Bergonzo and I. W. Boyd. *Microelectron. Eng.* **25**, 345 (1994).
57. T. Kanata, H. Takakura, Y. Hamakawa. *Appl. Phys. A* **49**, 305 (1989).
58. P. Bergonzo, U. Kogelschatz, I. W. Boyd. *Proc. Soc. Photo-Opt. Instrum. Eng.* (SPIE) - International Society for Optical Engineering **2045**, 174 (1994).
59. A. del Prado, M. Mártil, M. Fernández, G. González-Díaz. *Thin Solid Films* **343–344**, 437–440 (1999).
60. M. Boudreau, M. Boumerzoug, R. V. Kruzelecky, P. Mascher, P. E. Jessop, D. A. Thompson. *Mater. Res. Soc. Symp. Proc.* **300**, 183 (1993).
61. J. N. Cox, L. B. Friedrich, L. L. Heath, B. L. Sun. *J. Vac. Sci. Technol. B* **7** (3), 429 (1989).
62. S. K. Ray, S. Das, C. K. Maiti, S. K. Lahiri, N. B. Chakraborti. *J. Appl. Phys.* **75** (12), 8145 (1994).

63. S. K. Ray, S. Das, C. K. Maiti, S. K. Lahiri, N. B. Chakrabarti. *Appl. Phys. Lett.* **58** (22), 2476 (1991).
64. S. S. Chao, J. E. Tyler, D. V. Tsu, G. Lucovsky, M. J. Mantini. *J. Vac. Sci. Technol. A* **5** (4), 1283 (1987).
65. S. V. Nguyen, J. R. Abernathey, S. A. Fridmann, M. L. Gibson. 4th International Symposium on Semiconductor Processing, *ASTM Special Technical Publication* **960**, Emerging Semiconductor Technology, 173 (1987).
66. M. D. Diatezua, A. Dereux, A. Ronda, J. P. Vigneron, Ph. Lambin, R. Caudano. *Soc. Photo-Opt. Instrum. Eng.* (SPIE), **1149** (Optical Materials Technology for Energy Efficiency and Solar Energy Conversion VIII) 80 (1989).
67. M. D. Diatezua, P. A. Thiry, R. Caudano. *Vacuum* **46** (8–10), 1121 (1995).
68. T. S. Eriksson and C. G. Granqvist. *J. Appl. Phys.* **60** (6), 2081 (1986).
69. M. Firon, C. Bonnelle, A. Mayeux. *J. Vac. Sci. Technol. A* **14** (4), 2488–2492 (1996).
70. T. Ito, S. Hijiya, T. Nozaki, H. Arakawa, M. Shinoda, Y. Fukukawa. *J. Electrochem. Soc.* **125** (3), 448 (1978).
71. J. C. Rostaing, Y. Cros, S. C. Gujrathi, S. Poulain, *J. Non-Cryst. Solids* **97–98**, 1051 (1987).
72. W. M. Arnoldbik, C. H. M. Marée, F. H. P. M. Habraken. *Appl. Surf. Sci.* **74**, 103 (1994).
73. V. J. Kapoor and R. A. Turi. *Proc. Electrochem. Soc.* **89-7** (Proc. Symp. Silicon Nitride Silicon Dioxide Thin Insul. Films 1988), 19 (1989).
74. S. Neogi and D. A. Gulino. *Mater. Manuf. Processes* **6** (3), 433 (1991).
75. E. Baclez, B. Mutel, O. Dessaux, P. Goudmand, J. Grimblot, L. Gengembre. *Thin Solid Films* **303**, 156–166 (1997).
76. V. A. Burdovitsin, L. I. Rabinovich, K. I. Smirnova, T. P. Smirnova. *Inorg. Mater.* **12** (10), 1548 (1976).
77. F. Ansart and J. Bernard. *Phys. Sta. Sol. A* **134**, 134 (1992).
78. V. M. Bermudez. *Thin Solid Films* **347**, 195–200 (1999).
79. J. Yong Kim, M. A. Sriram, P. H. McMichael, N. P. Kumta, B. L. Phillips, S. H. Risbud. *J. Phys. Chem. B* **101** (24), 4689–4696 (1997).
80. *American Society of Metals Handbook, Vol. 10, Materials Characterisation* (1996).
81. S. Dreer. *Fresnius' J. Anal. Chem.* **365**, 85 (1999).
82. R. Dorka. IFW, Institute of Solid State Analysis and Structural Research, Dresden, Germany, private communications.
83. E. Mayer. Private communications.
84. S. Dreer. Ph.D. thesis, *Quantitative Characterisation of Silicon- and Aluminium Oxynitride Films Produced by Reactive dc-Magnetron Sputtering*, Vienna University of Technology (2000).
85. T. Ehara and S. Machida. *Thin Solid Films* **346**, 275–279 (1999).
86. K. J. Price, L. E. McNeil, A. Suvkanov, E. A. Irene, P. J. MacFarlane, M. E. Zvanut. *J. Appl. Phys.* **86** (5), 2628–2637 (1999).
87. O. Benkherourou and J. P. Deville. *Appl. Phys. A* **46**, 87 (1988).
88. Y. Okamoto, H. Nagasawa, D. Kitayama, H. Kitajima, H. Ikoma. *Jpn. J. Appl. Phys.* **34**, L955 (1995).
89. R. K. Brow and C. G. Pantano. *J. Am. Ceram. Soc.* **69** (4), 314 (1986).
90. J. R. Shallenberger, D. A. Cole, S. W. Novak. *J. Vac. Sci. Technol. A* **17** (4), 1086–1090 (1999).
91. N. Shibata. *Electronics and Communications in Japan*, Part 2, **75** (7), 84 (1992).
92. M. Bhat, G. W. Yoon, J. Kim, L. K. Han, J. Yan, D. Wristers, D. L. Kwong. *Proc. Electrochem. Soc.* **94-16**, 317 (1994).
93. L. K. Han, M. Bhat, D. Wristers, H. H. Wang, D. L. Kwong. *Microelectron. Eng.* **28**, 89 (1995).
94. J. F. Moulder, S. R. Bryan, U. Roll. *Fresenius' J. Anal. Chem.* **365**, 83 (1999).
95. J. Viard, E. Beche, D. Perarnau, R. Berjoan, J. Durand. *J. Eur. Ceram. Soc.* **17**, 2025–2028 (1997).
96. J. Viard, R. Berjoran, J. Durand. *J. Eur. Ceram. Soc.* **17**, 2001–2005 (1997).

97. J. C. Riviére, J. A. A. Crossley, B. A. Sexton. *J. Appl. Phys.* **64** (9), 4585 (1988).
98. M. S. Hegde, R. Caracciolo, K. S. Hatton, J. B. Wachtman, Jr. *Appl. Surf. Sci.* **37**, 16 (1989).
99. Y. Shima, H. Hasuyama, T. Kondoh, Y. Imaoka, T. Watari, K. Baba, R. Hatada. *Nucl. Instrum. Methods Phys. Res. B* **148**, 599–603 (1999).
100. S. Ogawa, Y. Suzuki, M. Yoshitake, K. Natsukawa. *IEEE*, 775–778 (1999).
101. Powder Diffraction File (PDF 2), International Centre for Diffraction Data, 12 Campus Boulevard, Newton Square, PA, USA.
102. M. Brunel, L. Ortega, Y. Cros, S. Viscaino. *Appl. Surf. Sci.* **65/66**, 289 (1993).
103. M. L. Monaghan, T. Nigam, M. Houssa, S. De Gendt, H. P. Urbach, P. K. de Bokx. *Thin Solid Films* **359**, 197–202 (2000).
104. S. C. Bayliss and S. J. Gurman. *J. Phys.: Condens. Matter* **6**, 4961 (1994).
105. J. I. Goldstein, S. K. Choi, F. J. J. Van Loo, H. J. M. Heijligers, G. F. Bastin, W. G. Sloof. *Scanning* **15**, 165 (1993).
106. G. F. Bastin and H. H. M. Heijligers. *Microbeam Anal.* **1**, 61 (1992).
107. J. M. Dijkstra, G. F. Bastin, H. J. M. Heijligers, D. Klepper. *Mikrochim. Acta* **114** (115), 277 (1994).
108. G. F. Bastin and H. J. M. Heijligers. *Mikrochim. Acta Suppl.* **12**, 19 (1992).
109. J. J. Goldstein, S. K. Choi, F. J. J. van Loo, H. J. M. Heijligers, J. M. Dijkstra, G. F. Bastin. *Microbeam Anal.* 57 (1991).
110. G. F. Bastin and H. J. M. Heijligers. *X-Ray Spectrometry in Electron Beam Instruments*, D. Williams, J. Goldstein, D. Newbury (Eds.), Chap. 14, p. 239, Plenum Press, New York (1995).
111. G. F. Bastin and H. J. M. Heijligers. *Microbeam Anal.* 207 (1989).
112. G. F. Bastin and H. J. M. Heijligers. *Scanning* **13**, 325 (1991).
113. T. Fuyuki, T. Saitoh, H. Matsunami. *Jpn. J. Appl. Phys.* **29** (10), 2247 (1990).
114. G. W. Vogl, K. H. Monz, Q. D. Nguyen, M. Huter, E. P. Rille, H. K. Pulker. *Soc. Photo-Opt. Instrum. Eng.* (SPIE) **2253**, 1275 (1994).
115. V. J. Silvestri, A. E. Irene, S. Zirinsky, J. D. Kuptsis. *J. Electron. Mater.* **4** (3), 429 (1975).
116. L. Pinard and J. M. Mackowski. *Appl. Opt.* **36** (22), 5451 (1997).
117. A. D. Mazzoni and E. F. Aglietti. *Sil. Ind.* **62** (7–8), 131–135 (1997).
118. S. Dreer, P. Wilhartitz, E. Mersdorf, G. Friedbacher. *Mikrochim. Acta* **130**, 281 (1999).
119. S. Dreer, P. Wilhartitz, E. Mersdorf, K. Piplits, G. Friedbacher. *Mikrochim. Acta* **131**, 211 (1999).
120. A. van Oostrom, L. Augustus, F. H. P. M. Habraken, A. E. T. Kuiper. *J. Vac. Sci. Technol.* **20** (4), 953 (1982).
121. J. Watanabe and M. Hanabusa. *J. Mater. Res.* **4** (4), 882 (1989).
122. H. Reinhardt, D. Schalch, A. Scharmann. *Thin Solid Films* **167**, L1 (1988).
123. B. C. Smith and H. H. Lamb. *J. Appl. Phys.* **83** (12), 7635 (1998).
124. H. H. Madden and P. H. Holloway. *J. Vac. Sci. Technol.* **16** (2), 618 (1979).
125. R. Hezel. *Radiat. Eff.* **65**, 101 (1982).
126. W. Streb and R. Hezel. *J. Vac. Sci. Technol. B* **2** (4), 626 (1984).
127. R. K. Pancholy and F. M. Erdmann. *IEEE Trans. Nucl. Sci.* **NS-30** (6), 4141 (1983).
128. T. Kaga and T. Hagiwara. *IEEE Trans. Electron Devices* **35** (7), 929 (1988).
129. Y. Saito. *Appl. Phys. Lett.* **68** (6), 800 (1996).
130. J. A. Nemetz and R. E. Tressler. *Solid State Technol.* **26** (2), 79 (1983).
131. R. B. Heimann. *J. Vac. Sci. Technol. B* **1** (1), 108 (1983).
132. S. Lim, J. H. Ryu, J. F. Wager, L. M. Casas. *Thin Solid Films* **236**, 64 (1993).
133. J. Flicstein, J. Mba, J.-M. Le Solliec, J. F. Palmier. *SPIE* **3091**, 72–82 (1997).
134. D. H. Wang and L. Guo. *Thin Solid Films* **198**, 207 (1991).
135. T. Jung. *Phys. Stat. Sol. A* **93**, 479 (1986).
136. L. U. J. T. Ogbuji and D. R. Harding. *Thin Solid Films* **263** (2), 194 (1995).

137. L. Martinu, J. E. Klemberg-Sapieha, O. M. Küttel, M. R. Wertheimer. *Annual Report: Conference on Electrical Insulation and Dielectric Phenomena*, IEEE, 178 (1990).
138. Y. B. Yankelevitch. *Vacuum* **30** (3), 97 (1979).
139. D. R. Harding, L. U. T. Ogbuji, M. J. Freeman. *J. Appl. Phys.* **78** (3), 1673 (1995).
140. L. N. Aleksandrov and F. L. Edelman. *Thin Solid Films* **66** (1), 85 (1980).
141. E. A. Irene, V. J. Silvestri, G. R. Woolhouse. *J. Electron. Mater.* **4** (3), 409 (1975).
142. F. Placido, J. Russell, Z. Gou. *SPIE* **2776**, 159–168 (1996).
143. A. von Richthofen and R. Dominick. *Thin Solid Films* **283**, 37 (1996).
144. M. D. Diatezua, P. A. Thiry, Ph. Lambin, R. Caudano. *Phys. Rev. B* **48** (12), 8701 (1993).
145. M. D. Diatezua, P. A. Thiry, G. Terwagne, R. Caudano. *Surf. Sci.* **269/270**, 1054–1059 (1992).
146. P. Poveda and A. Glachant. *Microelectron. Eng.* **28**, 357 (1995).
147. R. Franchy, G. Schmitz, P. Gassemann, F. Bartolucci. *Appl. Phys. A* **65**, 551–566 (1997).
148. F. Bartolucci, G. Schmitz, P. Gassemann, R. Franchy. *J. Appl. Phys.* **80** (11), 6467–6473 (1996).
149. A. E. T. Kuiper, M. F. C. Willemsen, J. M. L. Mulder, J. B. Oude Elferink, F. H. P. M. Habraken, W. F. van der Weg. *J. Vac. Sci. Technol. B* **7** (3), 455 (1989).
150. V. Gräfe, D. Schalch, A. Scharmann. *Phys. Stat. Sol. A* **117**, K23 (1990).
151. A. A. Saleh, J. B. Rothman, J. F. Kirchhoff, J. Yotab, C. Nguyen. *Thin Solid Films* **155–356**, 363–366 (1999).
152. M. F. Lambrinos, R. Valizadeh, J. S. Colligon. *Nucl. Instrum. Methods Phys. Res. B* **127/128**, 369–374 (1997).
153. M. Jacobs and F. Bodart. *Nucl. Instrum. Methods Phys. Res. B* **118**, 714–717 (1996).
154. L. Hrubcín, J. Huran, R. Šandrik, A. P. Kobzev, D. M. Shirokov. *Nucl. Instrum. Methods Phys. Res. B* **85**, 60 (1994).
155. C. H. M. Marée, W. M. Arnold Bik, F. H. P. M. Habraken. *Insulating Films on Semiconductors*, Proceedings from the 7th Biennial European Conference, 191 (1991).
156. L. G. Gosset, J.-J. Ganem, I. Trimaille, S. Sigo, F. Rochet, G. Dufour, F. Jolly, F. C. Stedile, I. J. R. Baumvol. *Nucl. Instrum. Methods Phys. Res. B* **136–138**, 521–527 (1998).
157. H. van Bebber, L. Borucki, K. Farzin, A. Z. Kiss, W. H. Schulte. *Nucl. Instrum. Methods Phys. Res. B* **136–138**, 72–76 (1998).
158. C. Rolfs and I. J. R. Baumvol. *Z. Phys. A: At. Nucl.* **353**, 127 (1995).
159. F. H. M. P. Habraken and A. E. T. Kuiper. *Thin Solid Films* **193/194** (1–2), 665 (1990).
160. O. Sanchez, J. M. Martinez-Duart, R. J. Gomez-Sanroman, R. Perez-Casero, M. A. Aguilar, C. Falcony, F. Fernandez-Gutierrez, M. Hernández-Vélez. *J. Mater. Sci.* **34**, 3007–3012 (1999).
161. T. D. M. Salagado, F. C. Stedile, C. Krug, I. J. R. Baumvol, C. Radtke. *Nucl. Instrum. Methods Phys. Res. B* **148**, 252–256 (1999).
162. I. J. R. Baumvol, F. C. Stedile, J.-J. Ganem, I. Trimaille, S. Rigo. *Appl. Phys. Lett.* **70** (15), 2007–2009 (1997).
163. A. Monelli, F. Corni, R. Tonini, C. Ferrari, G. Ottaviani, L. Zanotti, G. Queirolo. *J. Appl. Phys.* **80** (1), 109 (1996).
164. A. Sassella, A. Borghesi, F. Corni, A. Monelli, G. Ottaviani, R. Tonini, B. Pivac, M. Bachetta, L. Zanotti. *J. Vac. Sci. Technol. A* **15** (2), 377 (1997).
165. F. Corni, A. Monelli, G. Ottaviani, R. Tonini, G. Queirolo, L. Zanotti. *J. Non-Cryst. Solids* **216**, 71 (1997).
166. K. H. Ecker, U. Reinholz, M. Volbracht, H.-P. Weise. *Nucl. Instrum. Methods Phys. Res. B* **136–138**, 1277 (1998).
167. *Handbook of Modern Ion Beam Materials Analysis*, J. R. Tesmer and M. Nastasi (Eds.), MRS, Pittsburgh, PA (1995).
168. B. Semmache, M. Lemiti, Ch. Chanelière, Ch. Dubois, A. Sibai, B. Canut, A. Laugier. *Thin Solid Films* **296**, 32–36 (1997).
169. I. W. Boyd. *Mater. Sci. Forum* **173–174**, 81 (1995).

170. I. W. Boyd, J.-Y. Zhang, P. Bergonzo. *Proc. Soc. Photo-Opt. Instrum. Eng.* (SPIE) - International Society for Optical Engineering **2403**, 290 (1995).
171. R. I. Hedge, P. J. Tobin, K. G. Reid, B. Maiti, S. A. Ajuria. *Appl. Phys. Lett.* **66** (21), 2882 (1995).
172. Y. Okada, P. J. Tobin, R. I. Hedge, J. Liao, P. Rushbrook. *Appl. Phys. Lett.* **61** (26), 3163 (1992).
173. S. Singhvi and C. G. Takoudis. *J. Appl. Phys.* **82** (1), 442–448 (1997).
174. C. G. Sodini and K. S. Krisch. *Proceedings of the IEEE International Electron Device Meeting*, 617 (1992).
175. A. Hashimoto and M. Kobayashi. *OKI Technical Rev.* **52** (124), 49 (1986).
176. R. J. Hussey, T. L. Hoffman, Y. Tao, M. J. Graham. *J. Electrochem. Soc.* **143** (1), 221 (1996).
177. H. Ono, T. Ikarashi, Y. Miura, E. Haegawa, K. Ando, T. Kitano. *Appl. Phys. Lett.* **74** (2), 203–205 (1999).
178. F. Präßler, V. Hoffmann, J. Schumann, K. Wetzig. *J. Anal. At. Spectrom.* **10**, 677 (1995).
179. D. Rats, D. Poitras, J. M. Soro, L. Martinu, J. von Stebut. *Surf. Coat. Technol.* **111**, 220–228 (1999).
180. Ch. Chiang, G. Neubauer, A. Sauter Mack, K. Yoshioka, G. Cuan, P. A. Flinn, D. B. Fraser. *Mater. Res. Soc. Symp. Proc.* **265**, 219 (1992).
181. R. V. Smilgys, E. Takmura, I. L. Singer, S. W. Robey, D. A. Kirkpatrick. *Mater. Res. Soc. Symp. Proc.* **388**, 311 (1995).
182. E. Baclez, B. Mutel, O. Dessaux, P. Goudmand, J. Grimblot, L. Gengembre. *Thin Solid Films* **303**, 156–166 (1997).
183. N. Randall (Ed.). CSEM Instruments, Advanced Mechanical Surface Testing, Applications Bulletin 3 (1997), CSEM Instruments, Neuchâtel, Switzerland, <http://www.csem.ch/instrum>.
184. S. D. Dvorak, O. D. Greenwood, W. N. Unertl, R. J. Lad. *Mater. Res. Soc. Symp. Proc.* **522**, 439–444 (1998).
185. P. Ramminger, R. Krismer, P. Wilhartitz, R. Tessadri. *Proceeding of the 15th International Plansee Seminar*, G. Kneringer, P. Rödhammer, H. Wildner (Eds.), **4**, GT48, 216–228 (2001).
186. T. Kolber, K. Piplits, S. Dreer, E. Mersdorf, R. Haubner, H. Hutter. *Appl. Surf. Sci.* **167**, 79 (2000).